2

X-641-70-170
PREPRINT

NASA TM X-63926

MIE SCATTERING CALCULATIONS OF THE CONTRIBUTION OF ATMOSPHERIC AEROSOLS TO THE MARTIAN OPPOSITION EFFECT

JAYLEE MONTAGUE MEAD

JUNE 1970

GODDARD SPACE FLIGHT CENTER
GREENBELT, MARYLAND

MIE SCATTERING CALCULATIONS OF THE CONTRIBUTION OF ATMOSPHERIC AEROSOLS TO THE MARTIAN OPPOSITION EFFECT

Jaylee Montague Mead
Theoretical Studies Branch
Laboratory for Space Physics
Goddard Space Flight Center
Greenbelt, Maryland

June 1970

Submitted in partial fulfilment of the requirements for the degree of Doctor of Philosophy, Georgetown University, Washington, D. C.

MIE SCATTERING CALCULATIONS OF THE CONTRIBUTION OF ATMOSPHERIC AEROSOLS TO THE MARTIAN OPPOSITION EFFECT*

by

Jaylee Montague Mead

ABSTRACT

The Mie theory is used to compute the integrated scattering intensities for spherical submicron aerosol particles with various indices of refraction and several size distributions in an effort to determine if the presence of atmospheric aerosols can account for the Martian opposition effect, as observed by O'Leary and by Koval' in 1967. This nonlinear surge in brightness, as the planet approaches a phase angle of 0°, is reported to be much more pronounced in the ultraviolet than in the infrared.

The calculations show that neither substances having a refractive index n between 1.20 and 1.50, which include ice, water, and solid CO_2, nor highly absorbing materials, such as limonite, can produce the opposition effect. On the other hand, aerosols having $n > 1.50$ with little or no absorption, such as meteoric particles or suspended surface dust composed of semitransparent minerals, do exhibit a definite increase in reflectivity at small phase angles.

*A summary of this work appears in Icarus 13, No. 1 (1970).

By introducing an assumed surface function, which is added to the contribution by a layer of submicron-size aerosols with $\underline{n} = 1.65$, a model is obtained which compares reasonably well with the observations. In this model an atmospheric columnar density of 0.8×10^6 aerosols/cm^2 with average particle radius of 0.4μ gives the required aerosol contribution to the total reflectivity. Assuming a particle density of 2.5 gm/cm^3, this corresponds to a mass ratio of aerosols to gaseous atmosphere (for a Martian surface pressure of 7 mb) of 3×10^{-8}. Similar fits were obtained for $\underline{n} = 1.55$ and 1.75 and could probably be obtained for any real index between 1.55 and 1.75. This range includes most semitransparent minerals, thus making them good candidates for producing the opposition effect.

This study demonstrates that the presence of a small amount of atmospheric aerosols, with the proper index of refraction, could provide the observed increased opposition effect for Mars in the ultraviolet, where the albedo is very low and a small brightness contribution by aerosols will have a comparatively large effect, but at the same time make a negligible contribution in the infrared, where the surface albedo is high.

ACKNOWLEDGMENTS

I am especially grateful to the following people who have furthered the progress of this investigation: to the late Dr. Carl C. Kiess for introducing me to the study of Mars; to Rev. Francis J. Heyden, S.J., for his encouragement and support throughout my study at Georgetown University; to Dr. Paul D. Lowman, Jr., for help with basic mineralogy; to Dr. Bertram Donn, Dr. Robert Samuelson, and Dr. Walter Egan for useful discussions during the earlier phases of the light scattering calculations; to Dr. Louis Walter, Dr. John A. O'Keefe, and Dr. Lowman for critical comments on certain portions of the manuscript; to Mrs. Margaret Becker and her staff at the Goddard Space Flight Center for preparing the art work; to Mr. Thomas Michels for programming assistance; to the Goddard Space Flight Center for providing the computing facilities and employment opportunity to carry out this study; and especially to Dr. Gilbert Mead for careful reading of the manuscript.

TABLE OF CONTENTS

LIST OF TABLES

LIST OF ILLUSTRATIONS

LIST OF ILLUSTRATIONS (Continued)

CHAPTER I

INTRODUCTION: STATEMENT OF PROBLEM

Observations of Mars made by O'Leary (1967a, b) and by Koval' (1968) during the 1967 opposition show an "opposition effect", i.e., a nonlinear surge in brightness as the planet approaches 0° phase angle (the angle α at the planet between the directions to the Sun and to the observer). The effect is reported to be much more pronounced in the blue and ultraviolet than in the infrared. A strong opposition effect for the Moon had been well established earlier (e.g., Gehrels et al., 1964).

This increased opposition effect for Mars at shorter wavelengths could be primarily a surface effect in that the surface may have a much greater increase in reflectivity at these wavelengths; alternatively, it could be primarily due to light scattering in the atmosphere, as suggested by O'Leary (1967a).

Rayleigh scattering by molecules and by particles small compared to the wavelength of observation does not provide a sudden increase of brightness near 0° phase angle. Therefore, if the effect is primarily atmospheric, particles of larger size must be responsible.

The most convincing evidence for the presence of aerosols in the Martian atmosphere comes from the Mariner 7 television pictures (Leighton et al., 1969). A sharp haze or scattering layer can be seen adjacent to the limb of Mars in several frames. The scattering is

described as distinctly stratified in horizontal layers, similar to scattering from aerosol layers in the Earth's atmosphere.

Mars has a very low albedo in the ultraviolet, where the observed opposition effect is greatest; therefore, a small brightness contribution by atmospheric aerosols at these wavelengths will have a comparatively large effect. In the infrared, where the surface is much brighter, a small brightness contribution by aerosols will cause little or no change in the total brightness.

The purpose of this study is to investigate the contribution which atmospheric aerosols might make to the Martian opposition effect, under the assumption that the increased enhancement at shorter wavelengths, where the albedo is very low, is primarily an atmospheric effect rather than a surface effect. Here we define the term atmospheric aerosol as the particulate matter suspended in the planet's atmosphere.

The study is divided into four parts:

(1) Calculations of scattering intensity near 0° phase angle (180° scattering angle) by single spherical particles, using Mie scattering theory.

(2) Calculations of integrated intensities obtained by summing over particle-size distributions.

(3) Development of a model which incorporates an assumed surface photometric function plus an aerosol contribution, which is then compared with the observations.

(4) Examination of possible sources of Martian atmospheric aerosols.

CHAPTER II

OBSERVATIONAL DATA ON THE MARTIAN OPPOSITION EFFECT

Although there has been much photographic and photoelectric photometry of Mars, few of these measurements were made at small phase angles. Since the orbital plane of Mars is inclined at an angle of 1.85° to the ecliptic plane, the phase angle does not become very small for all oppositions. For example, α_{min} was only 4.5° during the opposition of 1939, 4.3° in 1956, and 3.0° in 1954. The situation was more favorable for obtaining data at small phase angles in 1952, 1958, and 1967 when α_{min} was 0.7°, 0.4°, and 1.2°, respectively. Unless a set of observations contains data for small phase angles, the "opposition effect" may go unnoticed.

The first indication of a possible brightening of Mars near opposition was reported by de Vaucouleurs (1959), based on his photoelectric photometry near the opposition of 1958. He found that the V magnitude of Mars at phase angles 6.8° and 10.2° was 0.05 to 0.1 mag brighter (at the same central longitude) than the values extrapolated from phase angle 21.4° with a linear phase law. A similar effect could be seen in the photoelectric photometry of Johnson and Gardiner (1955) during the 1954 opposition and in the photographic spectral photometry of Woolley (1953) and Woolley *et al.* (1955) during the 1952 and 1954 oppositions, as pointed out by de Vaucouleurs (1968) and Koval' (1968).

Additional evidence of the Martian opposition effect is given by Harris (1961), who states that the 1952 opposition observations from both the Mount Stromlo and McDonald Observatories showed Mars to be both brighter and bluer than normal on the night of May 3-4, 1952, when the phase angle was 2.5°; the ultraviolet magnitude was $0^m.3$ brighter, the blue magnitude about $0^m.2$ brighter, and the visual magnitude about $0^m.1$ brighter than expected by linear extrapolation.

Between 1962 and 1965 the Harvard College Observatory conducted an extensive program of multicolor photoelectric photometry of the brighter planets at its Boyden Observatory in South Africa and at the Le Houga Observatory in southern France (Irvine et al., 1968a, b). No anomalous brightening at opposition was found for the Martian opposition in 1965 (Irvine et al., 1968b). However, it has been reported that a subsequent re-examination of this data suggests that a small opposition effect may be evident (Irvine and Higdon, 1969).

During the opposition of 1967 Koval' (1968) made photoelectric observations of Mars in eight spectral regions ranging from 0.355μ to 0.619μ at the Kiev Observatory. He concluded that the brightness of Mars increased markedly with approach to $\alpha = 0^\circ$ in all the wavelength regions investigated. He also compared his data with that of Woolley et al. (1955) and Johnson and Gardiner (1955) and found good agreement with respect to the opposition effect. We have replotted the tabular data of the observed integrated albedo of Mars as a function of phase

angle from Koval' (1968, Table 1); the results are shown in Figure 1. On the right side of the figure, reflectivity P, or albedo, is shown on a logarithmic scale; its equivalent magnitude, given by

$$m = -2.5 \log_{10} P \qquad (1)$$

is shown on the left. To avoid prejudicing the reader, we have shown only the data points as given by Koval' in tabular form and refrained from drawing in a curve. For simplicity, we have included only four of the eight wavelengths at which observations were obtained. There is a definite increase in brightness at smaller phase angles (note in particular the observed values at 1.3°), and the effect appears to be more pronounced at shorter wavelengths than at longer ones.

O'Leary and Rea (1968) (see also O'Leary, 1967b) have also reported observations of Mars during the 1967 opposition, taken from Kitt Peak and Cerro Tololo, Chile. They, too, describe a definite opposition effect and note a more pronounced increase in reflectivity near opposition for shorter wavelengths than for longer ones.

Of the many programs which have been carried out for making photometric measurements of Mars, only the last three above have had sufficient coverage at small phase angles to permit a study of the opposition effect: O'Leary (1967b), Koval' (1968), and Irvine et al. (1968a, b) (the "Harvard program"). We shall now compare these three studies in order to point out the differences between them and to select the one most suitable for comparison with our theoretical calculations.

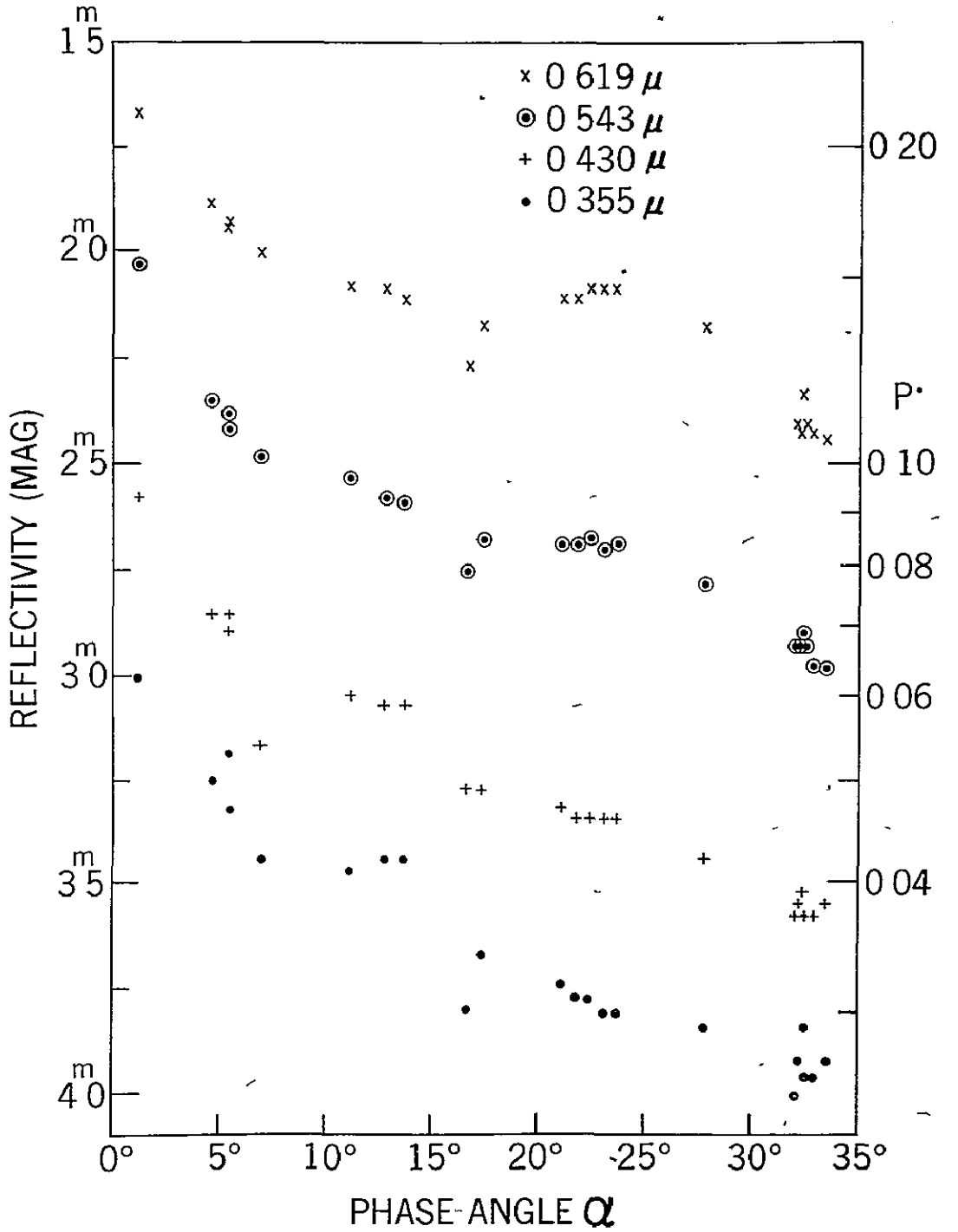

Figure 1. The observed integrated albedo of Mars, based on Koval' (1968, Table 1). Reflectivity, or albedo, is shown on a logarithmic scale on the right and on an equivalent magnitude scale on the left.

All of these observations were made with photoelectric multicolor photometers; however, the Koval' and Harvard programs used eight to ten narrow-band filters, averaging less than 0.015μ in bandwidth, whereas all of O'Leary's measurements were made with six or less broad-band filters, having bandwidths approximately 0.04μ.

The range in wavelengths covered in all three studies was approximately 0.36μ to 1μ with two exceptions: the filter of longest wavelength used by Koval' was centered at 0.619μ, while the Harvard program included a narrow-band filter at 0.3147μ.

The largest number of observations were reported in the Harvard study: 193 on 105 nights. Of these, only four points on two nights were obtained near the 1963 opposition and will, therefore, not be considered here. Forty-one observations at phase angles less than 13° were obtained during 16 nights near the 1965 opposition. The minimum phase angle observed in this series was 2.41°, and the maximum was 37.67°. There were eleven data points, covering five nights, which had phase angles less than 5°.

Koval' reported 23 mean observations for 22 nights, with eight nights having phase angles less than 13°. His range in phase angle was from 1.3° to 36.2°; however, only two (mean) data points were for phase angles less than 5°.

O'Leary listed 13 mean data points for 13 nights and stated that about 14 observations of Mars in each color were obtained on most of

these nights; however, no measurements were made for phase angles greater than 7.5°. He reported observations for nine nights when the phase angle was less than 5°; these means were presumably based on approximately 100 points.

The reflectivity of the Martian disk varies with longitude, depending on the predominance of bright or dark areas along the central meridian of observation. O'Leary (1967b) described how he corrected his data for this rotation effect. The other two studies do not mention any attempt to correct for this problem.

Because of the differences in techniques of reducing to absolute photometry, it is difficult to compare quantitatively these three studies or to merge all the data which covers a given opposition. It is unfortunate that O'Leary did not obtain more than 13 nights of observations, especially at phase angles greater than 7.5°, since this would have reduced the need for such a large extrapolation of his phase curve to that of other observers at larger phase angles. Despite this drawback, because his study has so many more data points at very small phase angles than do either Koval' or Irvine et al., O'Leary's observational data appears to be the better source to use for comparison with our theoretical calculations. We shall now review in greater detail the data obtained by O'Leary.

Figure 2 is taken from O'Leary and Rea (1968) and shows the Martian opposition effect in six colors: U, B, V, R, I, and I'. The observations, made at phase angles of 1.2° to 7.5°, are indicated by solid

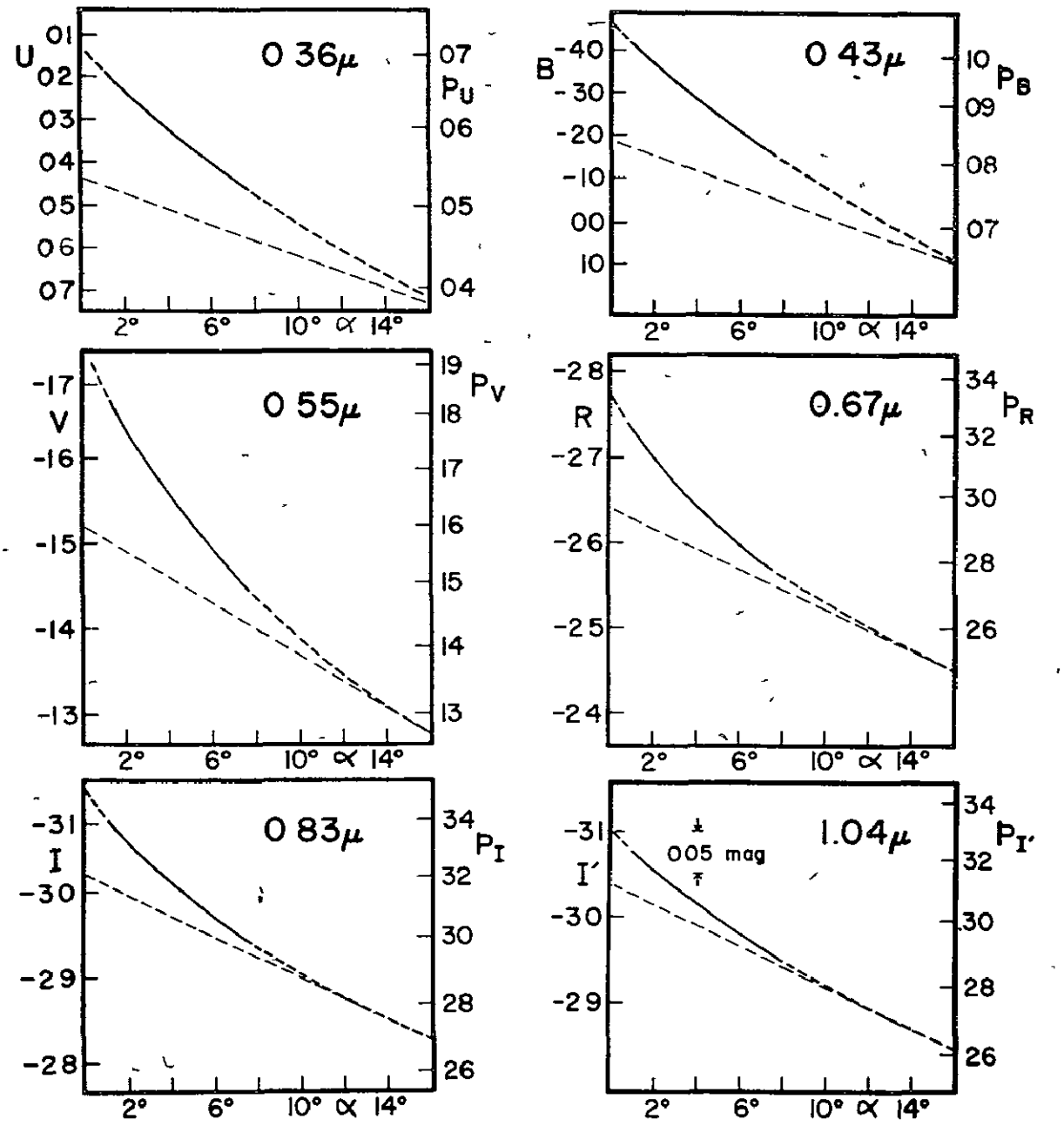

Figure 2. The Martian opposition effect in six colors fitted to the linear phase functions for $\alpha \gtrsim 10^{\circ}$ reported by de Vaucouleurs (1964). Values for the absolute magnitude are the ordinates on the left sides of the figures, and reflectivities normalized to geometric albedos are the ordinates on the right sides of the figures. (O'Leary and Rea, 1968).

lines. Each curve was determined by deriving the best curve through the observed data points and fitting this curve between $\alpha = 12^\circ$ and 16° (depending upon the wavelength) to the known linear phase function reported for $\alpha \geq 10^\circ$ (de Vaucouleurs, 1964). Note that the magnitude scales for the U and B curves at the top of Figure 2 are compressed by a factor of two compared to the other colors shown; the opposition effect for U and B is therefore greater than a first glance at these plots suggests.

In Figure 3 we plot the reflectivities from Figure 2, as adjusted for the color of the Sun, on a single continuous scale. On the right side of the figure, reflectivity P is shown on a logarithmic scale; its equivalent magnitude (see Equation 1) appears on the left. The reflectivity scale has a range of 2.5 magnitudes, or a factor of 10. As O'Leary and Rea pointed out, the opposition effect is much more pronounced at shorter wavelengths than at longer wavelengths, as evidenced by the fact that the U and B observations depart much more from the linear extrapolation than do the curves at R and I. The reflectivity, or albedo, on the other hand, is much greater at longer wavelengths than at shorter ones.

Table 1 expresses these concepts quantitatively. Note that the Bond albedo of Mars is only 5% in U, whereas it is 42% in I; yet the brightness increases by 72% from 16° to 0° phase angle in the U, but only 30% in the I.

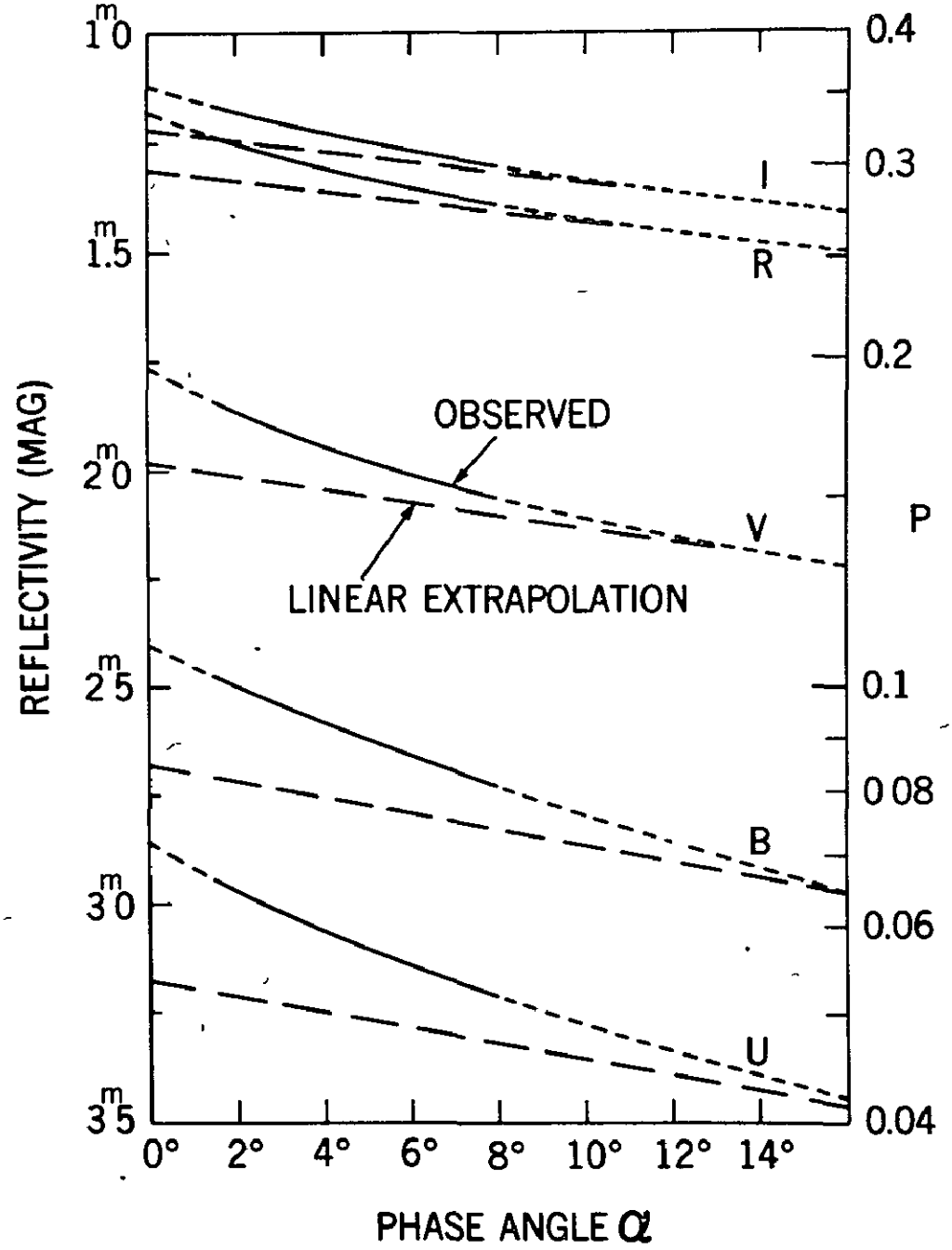

Figure 3. The Martian opposition effect, after O'Leary and Rea (1968), adjusted for the color of the sun. Reflectivity is shown on a logarithmic scale on the right and on an equivalent magnitude scale on the left.

TABLE 1

BOND ALBEDO AND OPPOSITION EFFECT FOR MARS
(after O'Leary, 1967b)

λ	Bond Albedo	Δm $(0^\circ - 16^\circ)$	P_{0°/P_{16°
U	0.05	0m59	1.72
B	0.08	0.56	1.68
V	0.17	0.45	1.52
R	0.38	0.32	1.34
I	0.42	0.29	1.30

CHAPTER LII

OBSERVATIONAL EVIDENCE FOR AEROSOLS IN THE MARTIAN ATMOSPHERE

There is considerable evidence, based primarily on observations of a variety of atmospheric formations, which suggests that aerosols are present in the Martian atmosphere. The clouds, veils, mists and hazes which have been reported on Mars are described by many authors (e.g., de Vaucouleurs, 1954; Dollfus, 1961; Hess, 1961; Kellogg and Sagan, 1961; Öpik, 1962; Slipher, 1962; Michaux, 1967; Glasstone, 1968). We shall first review the descriptions of the various atmospheric formations which have been reported from visual, photographic, photometric and polarimetric Earth-based observations. We shall then examine the Mariner 6 and 7 reports to see if similar phenomena are confirmed by the television pictures obtained from these missions. In each case we shall include only the descriptions of the observations, omitting the numerous theories which have been advanced to explain each phenomenon.

As early as 1858, A. Secchi reported observing white spots on the disk of Mars. W. R. Dawes noted a similar observation in 1864. It was not until 1877, however, that N. Green identified these spots as clouds. Since the spots appeared only on the limb of Mars and did not rotate with the planet, he concluded that they were not a surface feature, but must be atmospheric.

Yellowish clouds and veils were also reported by the early visual observers of Mars. Such observations were made with refracting telescopes, color-corrected for visual observing. Although color descriptions are quite subjective under such conditions, the differences in appearance between the yellow and white clouds were real enough to enable observers to definitely distinguish between the two kinds of clouds.

Three principal types of clouds are reported on Mars: "yellow" clouds, "white" clouds, and "blue" (or "violet") clouds, so named for the color of light which they predominantly reflect. In addition to the clouds, there is the so-called "blue haze", which is found on photographs taken in blue or ultraviolet light, but not detected at visual or longer wavelengths. We shall now summarize briefly the descriptions which observers have reported for these clouds and hazes.

(1) The yellow clouds are readily photographed in yellow or red light but are not seen in blue light. They may start out as an extensive obscuration and grow larger until they become a yellow "storm" covering most of the planet and lasting a month or more. Such was the case in 1924 and 1956. Or, they may appear as small, dense, orange or yellow formations lasting from one to four days. Occasional variations in photometric intensities or irregular polarization changes suggest that faint yellow veils may sometimes be present.

(2) The white clouds show wide variations in size and behavior.

Some are small bright formations which generally remain fixed in a given location. They may be surrounded by a large fainter cloud structure. The "polar hood" or "polar haze", which covers the polar cap during most of the local autumn and winter, is said to be composed of such small bright clouds.

During the Martian local spring and summer, when the polar cap in a given hemisphere is receding, white clouds or hazes are often seen at the sunrise edge of the planet. This morning haze remains stationary and extends for only a short distance across the planet. It usually occurs at low latitudes at about the same local time, but varies in size and intensity. In some regions the haze may appear several days in succession; in others, it is seen only occasionally. Such hazes are also observed to form near the evening terminator.

The largest white clouds have a tendency to occur above certain regions. Occasionally they show as bright prominences at the limb of the planet. They may remain visible for days or weeks. Large bright white clouds also appear at times over particular localities at low and medium latitudes in the late afternoon.

(3) The blue clouds are identified with the use of a blue filter, but they are less well defined as a definite class than the yellow and white clouds. Some observers believe that the blue and white clouds are the same phenomenon seen at different wavelengths, but others point to polarization and behavioral differences which they feel distinguish

the two types. Another classification associates the blue clouds with brighter areas in the blue haze.

(4) The blue haze is thought to be a tenuous atmospheric layer which contributes sufficiently to the atmospheric opacity so as to lower the surface contrast below the level where detail can be discerned in wavelengths of light shorter than about 0.455μ . Not all investigators are convinced that such a haze layer really exists; some attribute the lack of surface detail in blue light to decreased surface contrast in the blue and to poor seeing. Although most photographs of Mars in blue and ultraviolet light show little or no detail, at times one can obtain photographs at these wavelengths which reveal the surface features as clearly as in red light. Such a condition has been called a "blue-clearing". If this latter phenomenon is real, it is very hard to explain.

We now turn to the information on the Martian atmosphere obtained from the television experiments aboard the Mariner 6 and 7 spacecraft. The television cameras employed blue, green and red filters having effective wavelengths of 0.469μ , 0.526μ , and 0.573μ , respectively. The photographs obtained show surface features to be visible in all wavelengths, including the blue; therefore, the experimenters conclude that there is no obscuring "blue haze" (Leighton et al., 1969).

Hess (1970), Boyce (1970) and Öpik (1969) have questioned this interpretation and conclusion. All of these authors state that the

effective wavelength of the Mariner blue filters is too long to reveal the blue haze phenomenon. Furthermore, Hess claims that the features recorded by Earth-based telescopes are large compared with those recorded by the Mariner spacecraft. Therefore, since the telescopic features represent an average over the discrete elements photographed by the Mariners, they will be lower in contrast than those seen by the Mariners. Hence, a thin "blue haze" could exist which would obscure the large telescopic features while permitting the high-contrast small features to be recorded. Boyce describes his spectrophotometric measurements of Martian surface features, which show changes in contrast at short wavelengths. He interprets this as the variable opacity of a "violet" haze which is observed shortward of 0.43μ. Öpik points out that the computerized technique of eliminating background and noise, and the arbitrary enhancement of contrast, could cause craters to remain visible on the televised photographs even as far into the blue as 0.410μ. He recommends that future space photography of Mars include a filter at 0.365μ before the "blue haze" hypothesis is rejected. Thus the question of an obscuring haze at shorter wavelengths remains open.

The other atmospheric observations by the Mariners are less controversial, but in some cases just as perplexing. For instance, several <u>variable</u> bright features, which may be indicative of atmospheric processes, appeared in widely separated areas. The brightness of these

regions was observed to develop during the forenoon and to increase during the Martian afternoon. A similar phenomenon of local diurnal brightening had been noted earlier in descriptions of Earth-based observations of the white clouds observed on Mars. No fully satisfactory explanation for the effect is yet known.

The Mariners 6 and 7 flew by Mars slightly less than a week apart, yet marked changes in the brightness of some areas in the high northern latitude regions seem to have occurred during this period (Leighton et al., 1969, see Figure 7), which could be atmospheric effects. In addition, a diffuse brightening was observed to cover much of the north polar cap region. This presumably corresponds to the "polar hood", which has been observed from the Earth at this Martian season (northern early autumn).

Another possible indication of atmospheric haze is the observed darkening of the south polar cap near both the limb and terminator on the far-encounter pictures of Mariner 7. The experimenters point out that this darkening is definitely not due to cloud or thick haze since, during near-encounter, surface features were clearly visible everywhere over the polar cap. They suggest that the darkening may be due to optically thin aerosol scattering over the polar cap, or possibly to unusual photometric behavior of the cap itself.

The most clear-cut evidence for scattering layers in the Martian atmosphere is seen in a number of the Mariner 7 photographs which show

a sharp haze layer adjacent to the limb at several latitudes (Leighton et al., 1969, see especially Figure 4). Preliminary analysis of these pictures reveals stratified horizontal scattering layers similar to the aerosol layers in the Earth's atmosphere. A substantial variation in the scattering intensity over distances of a few hundred kilometers has been noted, with a greater intensity toward the west, i.e., toward earlier local times of day. The thickness of the layer was estimated to be about 10 km with heights between 15 and 40 km. The layer was reported to be about 50% brighter in the blue-filter pictures than in the red or green. An apparent limb haze was also observed near the south polar cap and in some nearby regions, but it was not as bright as the haze just described. A faint limb haze is thought to be present in the Mariner 6 limb pictures, also.

CHAPTER IV

LIGHT SCATTERING BY SINGLE PARTICLES (MIE THEORY)

The scattered light which is observed from a clear sky is due to two sources: (1) scattering by the air molecules and (2) scattering by atmospheric aerosols (haze and dust).

The molecular scattering can be treated by the Rayleigh scattering law (van de Hulst, 1957, p. 65). When unpolarized light of intensity I_o is incident upon a particle (molecule) whose radius is very small compared to the wavelength of observation, the intensity I of the radiation scattered in the direction θ and at a distance r from the particle is given by

$$I = \frac{8\pi^4 I_o}{\lambda^4 r^2} |\omega|^2 (1+\cos^2\theta) \qquad (2)$$

where λ is the wavelength of incident light in the surrounding medium and ω is the polarizability of the particle. The scattering angle θ is the angle between the direction of propagation of the incident wave and the scattered wave, and for single scattering is equal to $180^\circ - \alpha$, where α is the phase angle.

This Rayleigh scattering formula is valid for molecules and aerosols with radii less than about 0.1 times the wavelength of light. The entire phase angle dependence is contained in the $(1 + \cos^2\theta)$ term. This term has zero slope at 0° phase angle ($\theta = 180^\circ$), and is

reduced by only 3%, or $0^m.04$, at 15° phase angle; therefore, molecular scattering alone cannot account for the observed Martian opposition effect.

We next consider the second source of atmospheric scattering: aerosols. Very small aerosols, as mentioned above, follow Rayleigh's scattering law; particles of sizes greater than about 0.03μ radius must, however, be treated according to the exact diffraction theory.

The complete problem of diffraction of a plane wave by a homogeneous sphere of any composition has been treated rigorously by Gustav Mie (1908), according to the methods of classical electromagnetic theory. As a first approximation, most aerosols can be considered as spheres; thus Mie's formulae should give reasonably accurate results for such particles.

According to the Mie theory, if unpolarized light of intensity I_0 is incident upon a spherical aerosol particle of radius a, the intensity I of the radiation scattered in the direction θ and at a distance r from the particle is given by

$$I = \frac{I_0 \lambda^2}{8\pi^2 r^2} \left[i_1(x, \tilde{m}, \theta) + i_2(x, \tilde{m}, \theta) \right] \qquad (3)$$

where $x = 2\pi a/\lambda$ is the size parameter; $\tilde{m} = n - ik$ is the complex index of refraction of the scattering particle ($k = 0$, if non-absorbing; $k > 0$, if absorbing); and i_1 and i_2 are dimensionless intensity functions which refer, respectively, to the intensity of light vibrating

perpendicularly and parallel to the plane through the directions of propagation of the incident and scattered beams. Note that the particle radius a and the wavelength λ enter these intensity functions only through the size parameter x. (For a comprehensive treatment of the Mie theory, see van de Hulst (1957, especially pp. 35, 119-126).)

The intensity functions i_1 and i_2 were derived by Mie in terms of the complex amplitude functions S_1 and S_2:

$$i_1 = |S_1(x, \tilde{n}, \theta)|^2 \tag{4}$$

$$i_2 = |S_2(x, \tilde{n}, \theta)|^2 \tag{5}$$

where

$$S_1 = \sum_{m=1}^{\infty} \frac{2m+1}{m(m+1)} \left[a_m(x, \tilde{n}) \pi_m(\cos\theta) + b_m(x, \tilde{n}) \tau_m(\cos\theta) \right] \tag{6}$$

$$S_2 = \sum_{m=1}^{\infty} \frac{2m+1}{m(m+1)} \left[b_m(x, \tilde{n}) \pi_m(\cos\theta) + a_m(x, \tilde{n}) \tau_m(\cos\theta) \right] \tag{7}$$

The phase functions, π_m and τ_m, depend only on the scattering angle θ:

$$\pi_m = \frac{d P_m(\cos\theta)}{d\cos\theta} \tag{8}$$

$$\tau_m = \cos\theta \cdot \pi_m(\cos\theta) - \sin^2\theta \frac{d\pi_m(\cos\theta)}{d\cos\theta} \tag{9}$$

where $P_m(\cos\theta)$ are the Legendre polynomials.

The complex functions a_m and b_m are the so-called Mie coefficients, which can be interpreted physically as the m^{th} electrical partial wave and m^{th} magnetic partial wave, respectively:

$$a_m = \frac{\psi_m'(\tilde{n}x)\psi_m(x) - \tilde{n}\psi_m(\tilde{n}x)\psi_m'(x)}{\psi_m'(\tilde{n}x)\zeta(x) - \tilde{n}\psi_m(\tilde{n}x)\zeta'(x)} \tag{10}$$

$$b_m = \frac{\tilde{n}\psi_m'(\tilde{n}x)\psi_m(x) - \psi_m(\tilde{n}x)\psi_m'(x)}{\tilde{n}\psi_m'(\tilde{n}x)\zeta(x) - \psi_m(\tilde{n}x)\zeta_m'(x)} \tag{11}$$

where

$$\psi_m(z) = z j_m(z) = \left(\frac{\pi z}{2}\right)^{\frac{1}{2}} J_{m+\frac{1}{2}}(z) \tag{12}$$

$$\zeta_m(z) = z h_m^{(2)}(z) = \left(\frac{\pi z}{2}\right)^{\frac{1}{2}} H_{m+\frac{1}{2}}^{(2)}(z) \tag{13}$$

and a prime denotes differentiation with respect to the given argument. These are the Riccati-Bessel functions, derived either from the spherical Bessel functions of first and second kind, j_m and $h_m^{(2)}$, or from the half-integral Bessel functions, $J_{m+\frac{1}{2}}$ and $H_{m+\frac{1}{2}}^{(2)}$.

Equations (3)-(13) have been used to make light scattering calculations for substances including ice, water, and solid CO_2, which have no significant absorption in the wavelength range under consideration, and for highly absorbing materials, such as limonite.

The refractive indices covered by the calculations ranged from 1.20 to 2.40 in steps of 0.05. Indices with no absorption ($\underline{k} = 0$), small absorption ($\underline{k} = 0.01$ and 0.03) and large absorption ($\underline{k} \geq 0.1$) were considered. Of special interest for studies of Mars are the results obtained for the following refractive indices: 1.31 (ice), 1.33 (water), 1.35 (solid CO_2: Egan and Spagnolo, 1969), and $2.23 - 0.669\underline{i}$ (limonite at $\lambda = 0.365\mu$: Egan and Becker, 1969). The maximum size parameter examined was $\chi = 83$; however, the current study has been restricted to submicron particles. Phase angles as large as 60° have been considered, although the maximum phase angle at which Mars is observable from earth is $\sim 47^\circ$.

Figure 4 shows the computer printout of the sum of the intensity functions, $i_1 + i_2$, for a sphere of refractive index 1.35 with no absorption. All quantities were calculated and stored in floating point, but to conserve space on the printout the values were rounded to the nearest integer. The first column lists the size parameter ψ in increments of 0.4. The radii scales which correspond to the wavelengths 0.36μ (U), 0.55μ (V), and 0.83μ (I) are given in the next three columns. The remaining columns give the total intensity as a function of phase angle. Note that these values do <u>not</u> include the λ^2 factor of Equation (3).

We wish to examine the printout of Figure 4 to determine which particle radii, if any, show an increased enhancement in intensity at

(I1+I2) FOR PARTICLE RADIUS VS PHASE ANGLE
INDEX OF REFRACTION = 1.35

SIZE PARAM X	WAVELENGTH U(36)	V(55)	I(83)	PHASE ANGLE (DEG) 0	2	4	6	8	10	12	14	16	18	20	22	24	26	28	30	32	34	36	38	40
	RADII (MICRON)																							
0 1	0 021	0 035	0.059	0	0	0	0	0	0	0	0	0	0	0	0	0	0	0	0	0	0	0	0	0
0 2	0 042	0 070	0 106	0	0	0	0	0	0	0	0	0	0	0	0	0	0	0	0	0	0	0	0	0
1 2	0 069	0 105	0 159	0	0	0	0	0	0	0	0	0	0	0	0	0	0	0	0	0	0	0	0	0
1 6	0 092	0 140	0.211	0	0	0	0	0	0	0	0	0	0	0	0	0	0	0	0	0	0	0	0	0
2 0	0 115	0 175	0 264	0	0	0	0	0	0	0	0	0	0	0	0	0	0	0	0	0	0	0	0	0
2 4	0 138	0 210	0 317	1	1	1	1	1	1	1	1	1	1	1	1	1	1	1	1	1	1	0	0	0
2 8	0 138	0 245	0 370	1	1	1	1	1	1	1	1	1	1	1	1	1	1	1	0	0	0	0	0	0
3 2	0 183	0 280	0 423	1	1	1	1	1	1	1	1	1	1	1	1	1	1	0	0	0	0	0	0	0
3 6	0 206	0 315	0.476	3	3	3	3	3	3	3	3	3	2	2	2	2	2	2	2	2	2	1	1	1
4 0	0 229	0 350	0 528	2	2	2	2	2	2	1	1	1	1	1	1	1	1	1	1	1	2	2	2	2
4 4	0 252	0 385	0.581	4	4	4	4	4	4	3	3	3	2	2	2	2	2	2	2	2	2	2	2	2
4 8	0 275	0 420	0 634	7	6	6	6	6	6	5	5	5	4	4	4	4	4	4	4	4	4	4	4	4
5 2	0 298	0 455	0.687	3	3	3	3	3	2	2	2	2	2	3	3	3	4	5	5	6	6	7	7	7
5 6	0 321	0 490	0 740	9	9	9	8	8	7	6	6	5	5	5	6	6	6	7	7	7	7	7	6	5
6 0	0 344	0 525	0.791	7	7	7	7	6	6	6	6	7	7	8	10	11	11	12	12	12	11	10	8	7
6 4	0 367	0 560	0 845	6	6	5	5	4	4	4	4	6	7	9	11	13	15	16	16	15	14	12	10	9
6 8	0 390	0 595	0 898	10	10	10	9	8	8	8	9	10	12	14	15	16	17	16	14	12	9	6	4	3
7 2	0 413	0 630	0 951	5	5	4	4	4	5	8	11	16	21	25	29	31	31	29	25	20	15	11	7	5
7 6	0 435	0 665	1 004	6	5	5	4	4	5	7	11	16	20	24	27	27	26	22	18	13	10	8	7	8
8 0	0 458	0 700	1 057	10	10	9	8	8	11	15	22	30	37	41	42	40	33	25	16	9	5	5	7	12
8 4	0 481	0 735	1.110	1	1	1	2	4	9	17	26	36	44	48	48	43	35	26	17	11	9	10	12	16
8 8	0 504	0 770	1.162	17	16	13	11	11	16	25	36	48	55	57	52	42	29	17	10	9	14	23	31	37
9 2	0 527	0 805	1 215	2	2	2	3	8	18	32	46	58	64	62	52	38	23	11	6	8	15	23	30	32
9 6	0 550	0 840	1 268	19	18	14	13	18	30	50	71	87	93	86	69	47	27	16	16	24	35	43	43	37
10 0	0 573	0 875	1 321	18	17	14	13	17	29	46	62	71	69	56	37	19	8	9	20	36	50	56	52	40
10 4	0 596	0 910	1 374	19	17	13	14	27	52	84	112	125	117	91	56	26	11	14	30	48	58	55	42	25
10 8	0 619	0 945	1 427	65	61	51	43	44	57	75	90	91	77	52	28	14	18	35	55	68	66	51	29	12
11 2	0 642	0 980	1 480	41	37	24	28	43	75	111	134	131	101	58	21	9	23	54	83	93	82	55	29	15
11 6	0 665	1 015	1.532	110	102	83	67	68	85	109	121	110	78	40	15	13	32	57	71	65	43	20	10	18
12 0	0 688	1 050	1 585	86	78	63	58	76	113	148	158	139	83	37	19	37	76	109	114	88	48	17	10	24
12 4	0 710	1 085	1 638	148	133	100	73	74	99	128	133	105	57	18	10	35	77	94	87	58	30	21	35	57
12 8	0 733	1.120	1 691	75	89	71	74	107	157	191	182	130	64	23	28	66	102	106	76	34	11	21	51	75
13 2	0 756	1.155	1 744	274	245	179	120	104	124	146	134	87	35	18	48	101	135	124	79	33	18	36	62	69
13 6	0 779	1 190	1 797	71	63	53	69	120	180	203	167	91	26	13	51	100	118	92	49	27	40	70	85	69
14 0	0 802	1 225	1.849	463	411	291	183	140	151	161	127	63	19	34	92	139	132	78	25	17	54	97	104	72
14 4	0 825	1 261	1 902	90	80	68	89	145	199	200	138	59	23	54	116	149	125	70	32	35	62	73	53	20
14 8	0 848	1 296	1.955	528	455	294	164	134	171	186	133	51	13	46	103	117	76	30	38	97	152	147	88	27
15 2	0 871	1 331	2 008	124	112	99	124	183	225	200	117	45	41	95	141	128	70	24	27	63	84	67	33	18
15.6	0 894	1.366	2 061	541	449	259	130	140	215	230	150	54	34	85	127	105	54	46	98	149	136	67	15	26
16 0	0 917	1 401	2 114	83	74	74	120	195	230	180	81	20	39	95	114	79	39	46	90	117	95	47	19	24
16 4	0 940	1 436	2.166	688	566	317	156	167	237	223	119	43	67	133	140	79	32	57	110	114	64	31	63	120
16 8	0 963	1.471	2 219	30	27	46	119	212	238	155	62	24	69	120	116	77	65	95	118	93	40	13	28	50
17 2	0 985	1.506	2 272	762	615	320	141	159	222	179	66	19	70	117	88	36	51	126	151	109	59	66	101	93
17 6	1 008	1 541	2.325	37	37	67	157	252	257	161	62	53	109	134	97	54	57	84	80	48	34	58	83	70
18 0	1.031	1 576	2 378	582	442	187	91	190	274	201	64	16	56	77	55	67	138	184	141	64	44	75	81	46
18 4	1 054	1 611	2.431	29	30	68	167	256	233	116	31	49	104	103	56	41	74	100	87	70	79	90	66	24
18 8	1.077	1.646	2 483	418	299	110	108	267	337	218	64	26	63	69	57	86	127	109	57	57	111	134	91	45
19.2	1 100	1 681	2.536	1	5	54	167	260	203	77	19	67	122	109	77	91	122	115	79	62	65	53	30	30
19 6	1 123	1.716	2 589	411	293	114	123	260	277	135	20	34	76	62	38	55	74	74	99	156	169	106	42	38
20 0	1 146	1 751	2 642	18	26	87	212	286	212	82	50	114	148	111	90	93	100	73	54	65	76	67	62	72
20 4	1.169	1.786	2 695	347	236	80	111	235	220	81	13	59	94	70	59	85	107	118	135	126	76	46	78	113
20 8	1 192	1 821	2.748	27	35	103	232	287	185	56	49	112	113	59	46	80	101	99	108	114	94	67	56	46

Figure 4. Scattering intensity, $(i_1 + i_2)$, for Mie aerosols of refractive index 1.35. The first column gives the Mie size parameter, $x = 2\pi a/\lambda$, where a = particle radius as given in the next three columns for the specified wavelengths.

small phase angles relative to the intensity at larger phase angles. Large amounts of numerical output such as this are very tedious to analyze by visual scanning, however. We, therefore, sought a method of presentation which would aid us in discriminating those refractive indices for which the total intensity at small phase angles exceeded that computed for larger phase angles.

Since the O'Leary-Rea observations begin to depart from linearity in the U and B at around 15° phase angle (see Figure 2), it would be useful to know which size parameters show a significant intensity increase at $\alpha < 15^{\circ}$, but at the same time display a decrease in intensity at $\alpha > 15^{\circ}$. To make this comparison more apparent, we normalized the data shown in Figure 4 by dividing the calculated scattering intensity for a particular size parameter ψ at each phase angle by the mean intensity, averaged over phase angles from 12° through 18°, for that size parameter. These normalized scattering intensities, multiplied by 10^{3}, are shown for refractive index 1.35 in Figure 5. The column headings are the same as those for Figure 4.

With Figure 5 it is much easier to see immediately which intensities exceed the intensities around phase angle 15° and which are less. At $\psi = 0.4$, where the scattering follows Rayleigh's law, there is only a 3% increase in intensity from 15° to 0° phase angle, as would be expected from Equation (2). It is only when the size parameter ψ increases to 3.2 that one sees any significant intensity enhancement at

NORMALIZED (I1+I2) FOR PARTICLE RADIUS VS. PHASE ANGLE
INDEX OF REFRACTION = 1.35

SIZE PARAM. X	WAVELENGTH U(.36)	V(.55)	I(81)	PHASE ANGLE (DEG) 0	2	4	6	8	10	12	14	16	18	20	22	24	26	28	30	32	34	36	38	40
	RADII (MICRON)																							
0.4	0.023	0.035	0.053	1033	1033	1031	1028	1024	1019	1012	1005	996	987	976	965	953	940	926	912	897	881	865	849	832
0.8	0.046	0.070	0.106	1026	1026	1024	1022	1019	1015	1010	1004	997	989	981	972	962	952	941	929	917	904	891	878	865
1.2	0.069	0.105	0.159	1013	1012	1012	1011	1009	1007	1005	1002	999	995	991	987	982	977	972	966	960	954	949	942	936
1.6	0.092	0.140	0.211	980	980	981	983	985	988	992	997	1002	1009	1016	1024	1034	1044	1056	1069	1084	1101	1119	1139	1162
2.0	0.115	0.175	0.264	1162	1159	1150	1135	1115	1089	1058	1022	982	938	891	841	788	735	681	626	573	522	473	428	387
2.4	0.138	0.210	0.317	1082	1080	1076	1069	1058	1045	1030	1011	991	968	943	916	888	858	827	794	761	728	694	661	627
2.8	0.160	0.245	0.370	1094	1092	1087	1077	1065	1049	1031	1011	990	968	946	924	904	885	870	857	849	844	844	849	858
3.2	0.183	0.280	0.423	1300	1294	1276	1247	1207	1158	1100	1036	968	895	822	750	680	616	557	507	467	437	419	414	421
3.6	0.206	0.315	0.476	1210	1206	1193	1173	1145	1110	1070	1026	977	927	875	824	773	725	680	638	600	566	536	510	488
4.0	0.229	0.350	0.528	1336	1328	1303	1264	1213	1153	1089	1026	967	918	882	862	862	883	925	986	1065	1158	1262	1370	1477
4.4	0.252	0.385	0.581	1520	1508	1472	1415	1339	1250	1151	1048	947	853	770	702	651	618	604	608	627	658	697	742	786
4.8	0.275	0.420	0.634	1351	1342	1315	1272	1218	1155	1089	1025	967	919	884	862	853	855	866	880	893	901	899	884	853
5.2	0.298	0.455	0.687	1538	1515	1461	1385	1241	1127	1032	974	969	1025	1147	1331	1568	1840	2127	2406	2653	2848	2973	3017	2977
5.6	0.321	0.490	0.740	1637	1616	1556	1463	1349	1228	1113	1018	951	919	921	954	1008	1072	1132	1177	1194	1178	1126	1042	934
6.0	0.344	0.525	0.793	1115	1102	1064	1011	957	918	909	940	1016	1135	1286	1453	1614	1748	1833	1853	1802	1679	1495	1268	1022
6.4	0.367	0.560	0.845	1121	1019	1001	883	771	707	715	834	1062	1388	1780	2193	2574	2874	3053	3087	2973	2732	2400	2025	1659
6.8	0.390	0.595	0.898	1062	1041	984	910	843	808	826	907	1045	1222	1409	1570	1671	1686	1604	1431	1191	918	656	444	315
7.2	0.413	0.630	0.951	360	347	316	291	304	385	553	811	1139	1497	1834	2096	2239	2235	2084	1811	1462	1094	765	523	395
7.6	0.435	0.665	1.004	414	394	345	298	293	369	544	815	1149	1492	1781	1959	1991	1869	1620	1299	972	706	549	520	605
8.0	0.458	0.700	1.057	391	373	333	301	316	409	593	853	1145	1409	1586	1627	1518	1277	955	622	350	193	175	285	479
8.4	0.481	0.735	1.110	46	40	33	53	134	299	550	857	1170	1424	1563	1555	1403	1144	841	564	369	286	310	403	515
8.8	0.504	0.770	1.162	406	378	314	260	270	383	601	884	1162	1354	1399	1279	1025	710	425	251	228	346	552	763	901
9.2	0.527	0.805	1.215	42	36	31	62	166	362	632	924	1163	1281	1239	1047	757	495	224	121	155	292	463	597	645
9.6	0.550	0.840	1.268	260	238	192	172	234	404	662	942	1159	1237	1146	916	624	365	218	211	315	461	568	580	488
10.0	0.573	0.875	1.321	297	272	221	204	281	473	741	998	1145	1115	909	599	304	133	148	327	486	810	905	838	645
10.4	0.596	0.910	1.374	176	156	121	132	247	476	767	1023	1141	1069	829	513	240	103	130	272	435	526	501	379	226
10.8	0.619	0.945	1.427	781	728	610	516	432	681	901	1076	1096	927	629	334	174	213	415	662	817	796	610	352	145
11.2	0.642	0.980	1.480	346	309	239	231	362	630	933	1125	1097	845	483	180	74	194	452	692	783	684	463	241	122
11.6	0.665	1.015	1.532	1054	974	792	646	651	819	1041	1156	1053	750	388	145	129	311	549	680	620	411	191	95	175
12.0	0.688	1.050	1.585	657	597	481	443	582	866	1136	1212	1016	636	281	146	286	585	836	871	672	364	128	75	186
12.4	0.710	1.085	1.638	1398	1258	943	694	698	939	1208	1259	993	539	168	94	330	681	891	823	550	280	199	332	541
12.8	0.733	1.120	1.691	671	609	504	523	755	1108	1350	1286	915	449	163	198	464	717	747	533	239	80	149	361	531
13.2	0.756	1.155	1.744	2737	2445	1780	1198	1032	1237	1453	1336	863	348	179	481	1009	1346	1238	785	334	184	358	615	684
13.6	0.779	1.190	1.797	584	515	431	563	982	1471	1666	1370	748	215	107	417	821	963	751	401	218	326	574	699	567
14.0	0.802	1.225	1.849	4498	4435	3142	1972	1508	1631	1738	1376	680	207	364	992	1503	1428	843	271	186	588	1047	1126	779
14.4	0.825	1.261	1.902	869	762	651	844	1384	1895	1903	1315	559	229	518	1105	1419	1194	668	304	336	585	693	504	194
14.8	0.848	1.296	1.955	5525	4761	3076	1712	1402	1789	1948	1392	528	133	480	1076	1226	794	318	394	1017	1585	1538	917	281
15.2	0.871	1.331	2.008	1230	1111	984	1227	1817	2232	1979	1162	450	410	940	1396	1272	696	234	266	620	829	663	328	176
15.6	0.894	1.366	2.061	4628	3846	2212	1114	1201	1842	1969	1281	463	287	725	1084	898	461	394	838	1277	1162	577	124	226
16.0	0.917	1.401	2.114	1043	932	926	1497	2437	2879	2248	1012	250	490	1189	1433	991	491	575	1128	1467	1185	583	232	300
16.4	0.940	1.436	2.166	6097	5022	2814	1385	1477	2102	1973	1054	379	594	1180	1244	700	286	504	973	1008	565	274	559	1065
16.8	0.963	1.471	2.219	378	339	571	1492	2653	2982	2065	770	306	859	1506	1457	965	811	1183	1474	1161	504	164	346	625
17.2	0.986	1.506	2.272	9163	7393	3846	1698	1917	2675	2152	789	223	836	1411	1057	431	608	1440	1821	1316	714	792	1211	1119
17.6	1.008	1.541	2.325	380	380	696	1633	2625	2677	1670	646	555	1129	1395	1008	560	598	873	836	494	350	604	864	730
18.0	1.031	1.576	2.378	6925	5262	2229	1088	2458	3259	2392	757	186	665	919	658	801	1646	2193	1675	762	525	892	968	542
18.4	1.054	1.611	2.431	386	403	902	2223	3398	3096	1545	418	657	1381	1365	751	545	983	1331	1161	925	1045	1190	881	319
18.8	1.077	1.646	2.483	4520	3230	1190	1171	2882	3642	2351	688	285	676	747	616	930	1369	1177	615	614	1203	1451	984	482
19.2	1.100	1.681	2.536	9	67	754	2337	3502	2842	1082	263	944	1710	1531	1085	1270	1714	1613	1107	868	909	750	423	426
19.6	1.121	1.716	2.589	6208	4423	1727	1864	3918	4182	2033	307	510	1150	933	578	826	1120	1121	1500	2351	2549	1608	635	574
20.0	1.146	1.751	2.642	183	259	883	2157	2902	2154	830	507	1158	1504	1128	809	940	1014	745	546	660	768	677	635	727
20.4	1.169	1.786	2.695	5614	3816	1296	1793	3801	3555	1305	216	962	1517	1136	953	1371	1723	1912	2182	2045	1236	738	1256	1833
20.8	1.192	1.821	2.748	331	431	1251	2821	3487	2251	679	592	1360	1369	714	555	977	1225	1208	1309	1391	1150	815	680	554

Figure 5. Scattering intensity, $(i_1 + i_2)$, for Mie aerosols of refractive index 1.35, normalized to the average intensity for $12° \leq \alpha \leq 18°$ and multiplied by 1000.

small phase angles. Between $3.2 \leq \psi \leq 4.8$, there is evidence of a small opposition effect, without an increase at larger phase angles, as can be confirmed from Figure 4, but this is only for a very limited particle size range (e.g., this would correspond to particle radii between 0.18μ and 0.28μ in U). From $5.2 \leq \psi \leq 7.6$, the largest intensities are at the <u>larger</u> phase angles instead of the smaller ones. Beyond this point, no definite pattern of enhancement is apparent.

Although the normalized intensities of Figure 5 are a definite aid in analyzing the light scattering calculations, we still have to examine each entry to determine the amplitude, or degree, of the effect. Furthermore, it is not easy to see major trends or groupings.

Our next step was, therefore, to convert the Figure 5 calculations to a schematic representation in terms of relative magnitudes. This was done according to the code given in Table 2. The resulting schematic representation of the scattering intensities for refractive index 1.35 is shown in Figure 6. Adjacent bars of the same kind, either vertical or horizontal, have been connected. Thus, in regions of continuous solid vertical bars (such as $6^\circ < \alpha < 12^\circ$ and $17 < \psi < 20$), the scattering intensity is at least $1^m.25$ <u>brighter</u> than the average scattering intensity from 12° to 18° phase angle for that size parameter. A dot indicates that the scattering intensity is within $\pm 0^m.125$ of the 12° to 18° average. A region of solid horizontal bars (such as for $0^\circ < \alpha < 8^\circ$ and $7 < \psi < 10$) shows that the scattering

TABLE 2

CODE USED FOR SCHEMATIC SCATTERING INTENSITY DIAGRAMS SHOWN IN FIGURES 6, 8, 10, 12, AND 14

Code	Normalized Scattering Intensity $(i_1 + i_2)$	Equivalent Magnitudes $m(\alpha) - m_{av}(12^\circ - 18^\circ)$
|||||	> 2818	$\leq -1.^m25$
||||	2240 - 2818	-1.00
|||	1779 - 2239	-0.75
||	1414 - 1778	-0.50
|	1123 - 1413	-0.25
•	892 - 1122	0.00
-	709 - 891	+0.25
—	563 - 708	+0.50
—	448 - 562	+0.75
—	355 - 447	+1.00
—	< 355	$\geq +1.25$

intensity is at least $1.^m25$ or more fainter than the average scattering intensity from 12° to 18°.

The usefulness of this display lies in allowing us to observe how the scattering intensity for a given particle radius and wavelength varies with phase angle, and thus to see quickly and easily which

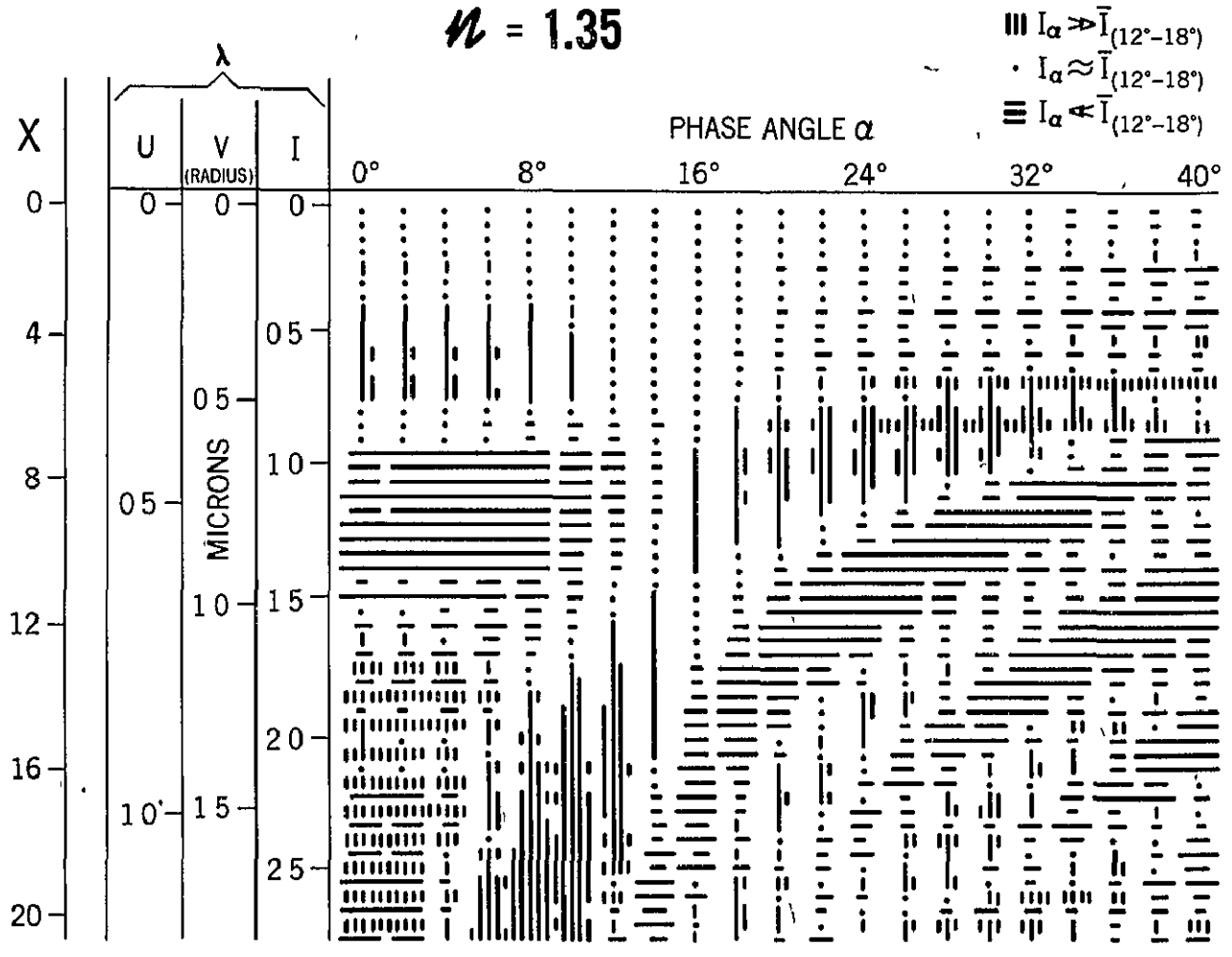

Figure 6. Schematic diagram of the scattering intensity for Mie aerosols of refractive index 1 35, normalized to the average intensity for $12^\circ \leq \alpha \leq 18^\circ$. The first column gives the Mie size parameter, $x = 2\pi a/\lambda$, where a = particle radius as given in the next three columns for wavelengths 0.36 (U), 0.55 (V), and 0 83 (I) micron. See Table 2 for code used to construct diagram

particle sizes show an increase in intensity, or brightness, near small phase angles, and which do not. As noted earlier, the Martian opposition effect is observed to depart from linearity around 15° phase angle in the U and B; therefore, we are looking for particle sizes which give an enhancement at small angles---that is, lots of vertical lines near 0° phase angle.

The same conclusions which we reached earlier based on the numerical output are even more readily apparent in Figure 6. There is a slight opposition effect around $\chi = 4$, but the intensity here is only about $\frac{1}{4}$ magnitude brighter than the average intensity around 15°, as indicated by the low density of vertical lines (see Table 2). For $8 \leq \chi \leq 12$, there is an anti-opposition effect, as evidenced by the large number of horizontal lines at small phase angles. Further down the diagram, at larger radii, where there is a spotty positive effect, the solid-line enhancement occurs for phase angles of 6° to 12°, which is not what the Mars observations show. It does not, therefore, appear that submicron spherical particles with refractive index 1.35 are good candidates for producing the opposition effect. Similar displays for refractive indices from 1.20 to 1.50 all produce only small variations of the basic picture seen in Figure 6.

As mentioned earlier, the refractive index of 1.35, for which the Figures 4 - 6 computations were made, is of particular interest for studies of Mars since it is the only measurement found in the literature

for solid CO_2 in the ultraviolet. These measurements, which were made by Egan and Spagnolo (1969) for bulk CO_2, cover the wavelength range 0.35 to 1.0μ and show little or no wavelength dependence. The absorption coefficient $\underline{k}$ reported by these authors is very small in this wavelength range and can be neglected in our calculations. Thin-film measurements of the refractive index for CO_2 cryodeposits by Tempelmeyer and Mills (1968) show slightly higher values for the real part of the refractive index and a variation with wavelength. They obtained a value of $\underline{n} = 1.455$ at $\lambda = 0.6\mu$, the shortest wavelength at which their measurements were reported; however, the slope of their curve at this point suggests that the index might be increasing toward shorter wavelengths. Egan and Spagnolo (1969) have suggested that the discrepancy in these measurements may be due to the difference in temperature (and therefore density) of the samples (77°K for Tempelmeyer and Mills vs. 195°K for Egan and Spagnolo); alternatively, surface or body scattering could reduce the observed Brewster angle, thus resulting in a slightly lower real portion of the index of refraction. Additional measurements of the refractive index of solid CO_2 over this range of temperature are desirable.

Figure 7 gives the computer output (not normalized) of scattering intensities for a highly absorbing material, limonite, using the complex refractive index in the ultraviolet as measured by Egan and Becker (1969). Here there is almost no change in scattering intensity with phase angle

(I1+I2) FOR PARTICLE RADIUS VS. PHASE ANGLE
INDEX OF REFRACTION = 2.23-0.669 I

WAVELENGTH = 0.36

SIZE PARAM X	RADII (MICRON)	PHASE ANGLE (DEG) 0	2	4	6	8	10	12	14	16	18	20	22	24	26	28	30	32	34	36	38	40
0.4	0.023	0	0	0	0	0	0	0	0	0	0	0	0	0	0	0	0	0	0	0	0	0
0.8	0.046	0	0	0	0	0	0	0	0	0	0	0	0	0	0	0	0	0	0	0	0	0
1.2	0.069	0	0	0	0	0	0	0	0	0	0	0	0	0	0	0	0	0	0	0	0	0
1.6	0.092	0	0	0	0	0	0	0	0	0	0	0	0	0	0	0	0	0	0	0	0	0
2.0	0.115	1	1	1	1	1	1	1	1	1	0	0	0	0	0	0	0	0	0	0	0	0
2.4	0.138	1	1	1	1	1	1	1	1	1	1	1	1	1	1	1	1	1	1	1	1	1
2.8	0.160	0	0	0	0	0	0	0	0	0	0	0	0	0	1	1	1	1	1	1	1	1
3.2	0.183	2	2	2	1	1	1	1	1	1	1	1	1	1	1	1	1	1	1	1	1	1
3.6	0.206	1	1	1	1	1	1	1	1	1	1	1	1	1	1	1	1	1	1	1	1	1
4.0	0.229	1	1	1	1	1	1	1	1	1	1	1	1	1	1	2	2	2	2	2	2	2
4.4	0.252	2	2	2	2	2	2	2	2	2	2	2	2	2	2	2	2	2	2	2	2	2
4.8	0.275	2	2	2	2	2	2	2	2	2	2	2	2	2	2	2	2	2	2	2	2	2
5.2	0.291	2	2	2	2	2	2	2	2	2	2	2	2	3	3	3	3	3	3	3	3	3
5.6	0.321	3	3	3	3	3	3	3	3	3	3	3	3	3	3	3	3	3	3	3	3	3
6.0	0.344	3	3	3	3	3	3	3	3	3	3	3	3	3	3	3	3	3	3	3	3	3
6.4	0.367	3	3	3	3	3	3	3	3	4	4	4	4	4	4	4	4	4	4	4	4	4
6.8	0.390	5	5	5	5	5	5	4	4	4	4	4	4	4	4	4	4	4	4	4	4	5
7.2	0.413	4	5	5	5	5	5	5	5	5	5	5	5	5	5	5	5	4	4	4	5	5
7.6	0.435	5	5	5	5	5	5	5	5	5	5	5	5	6	6	6	6	5	5	5	5	5
8.0	0.458	6	6	6	6	6	6	6	6	6	6	6	6	6	6	6	6	6	6	6	6	6
8.4	0.481	6	6	6	6	6	6	6	7	7	7	7	6	6	6	6	6	6	6	6	6	7
8.8	0.504	7	7	7	7	7	7	7	7	7	7	7	7	7	7	7	7	7	7	7	7	7
9.2	0.527	8	8	8	8	8	8	8	8	7	7	7	7	7	8	8	8	8	8	8	8	8
9.6	0.550	8	8	8	8	8	8	8	9	9	9	8	8	8	8	8	8	8	8	8	9	9
10.0	0.573	9	9	9	9	9	9	9	9	9	9	9	9	9	9	9	9	9	9	9	9	9
10.4	0.596	10	10	10	10	10	10	10	10	10	10	10	10	10	10	10	10	10	10	10	10	10
10.8	0.619	10	10	10	10	10	11	11	11	11	11	11	10	10	10	10	10	11	11	11	11	11
11.2	0.642	11	11	11	11	11	11	11	11	11	11	12	12	11	11	11	11	11	11	11	11	11
11.6	0.665	13	13	13	12	12	12	12	12	12	12	12	12	12	12	12	12	12	12	12	12	12
12.0	0.688	13	13	13	13	13	13	13	13	13	13	13	13	13	13	13	13	13	13	13	13	13
12.4	0.710	14	14	14	14	14	14	14	14	14	14	14	14	14	14	14	14	14	14	14	14	14
12.8	0.733	15	15	15	15	15	15	15	15	15	15	15	15	15	15	15	15	15	15	15	15	15
13.2	0.756	15	15	15	16	16	16	16	16	16	16	16	16	16	16	16	16	16	16	16	16	16
13.6	0.779	17	17	17	17	17	17	17	17	17	17	17	17	17	17	17	17	17	17	17	17	17
14.0	0.802	18	18	18	18	18	18	18	17	17	18	18	18	18	18	18	18	18	18	18	18	18
14.4	0.825	18	18	18	19	19	19	19	19	19	19	19	19	19	19	19	19	19	19	19	19	19
14.8	0.848	20	20	20	20	20	20	20	20	20	20	20	20	20	20	20	20	20	20	20	20	20
15.2	0.871	21	21	21	21	21	21	21	21	21	21	21	21	21	21	21	21	21	21	21	21	21
15.6	0.894	22	22	22	22	22	22	22	22	22	22	22	22	22	22	22	22	22	22	22	22	22
16.0	0.917	23	23	23	23	23	23	23	23	23	23	23	23	23	23	23	23	23	23	23	23	23
16.4	0.940	25	25	24	24	24	24	24	24	24	24	24	24	24	24	24	24	24	24	24	25	24
16.8	0.963	25	25	25	25	26	26	26	26	25	25	25	25	25	26	26	26	25	25	25	25	26
17.2	0.985	27	27	27	27	27	27	27	27	27	27	27	27	27	27	27	27	27	27	27	27	27
17.6	1.008	28	28	28	28	28	28	28	28	28	28	28	28	28	28	28	28	28	28	28	28	28
18.0	1.031	29	29	29	29	29	29	29	29	29	29	29	29	29	29	29	29	29	29	29	29	29
18.4	1.054	31	31	31	31	30	30	31	31	31	31	30	30	30	31	31	31	31	31	30	30	31
18.8	1.077	32	32	32	32	32	32	32	32	32	32	32	32	32	32	32	32	32	32	32	32	32
19.2	1.100	33	33	33	33	33	33	33	33	33	33	33	33	33	33	33	33	33	33	33	33	33
19.6	1.123	35	35	35	35	35	35	35	35	35	35	35	35	35	35	35	35	35	35	35	35	35
20.0	1.146	36	36	36	36	36	36	36	36	36	36	36	36	36	36	36	36	36	36	36	36	36
20.4	1.169	37	37	37	38	38	38	38	38	37	37	38	38	38	38	37	37	37	38	38	38	38
20.8	1.192	39	39	39	39	39	39	39	39	39	39	39	39	39	39	39	39	39	39	39	39	39

Figure 7. Same as Figure 4, except $\tilde{n} = 2.23 - 0.669i$, $\lambda = 0.36$ micron.

for a given particle radius. The schematic diagram for these calculations is shown in Figure 8. The almost total absence of enhancement anywhere is striking. Thus aerosols of limonite, or of any other highly absorbing substance, could not produce an opposition effect. Similar results were found for all absorbing refractive indices where $\underline{k} \geq 0.1$.

Figure 9 shows the scattering intensities for $\underline{n} = 1.55$. The enhancement at small phase angles is immediately obvious. The schematic diagram for $\underline{n} = 1.55$, Figure 10, looks considerably different from either of the previous schematic displays (see Figures 6 and 8). There is a strong continuous enhancement from 0° to 10° phase angle, with very small contributions at larger phase angles, for $3 \leq \psi \leq 11$. This size parameter corresponds to particle radii in the U ranging from around 0.2 to 0.7μ. We can see that this same particle radii range would show a smaller enhancement in the V and much less in the I.

Indications of an even more significant opposition effect are exhibited by calculations for aerosols having refractive indices of 1.65 and 1.75, as shown in Figures 11 - 14. In the case of $\underline{n} = 1.65$, Figure 12 shows that the opposition effect is evident for size parameter $\psi = 4$ and greater. This intensity enhancement begins to be noticeable at around 12° phase angle and gradually increases in magnitude until around $\alpha = 4^\circ$, where it becomes much more pronounced and continues on through 0° phase angle. If we compare the scattering intensities from

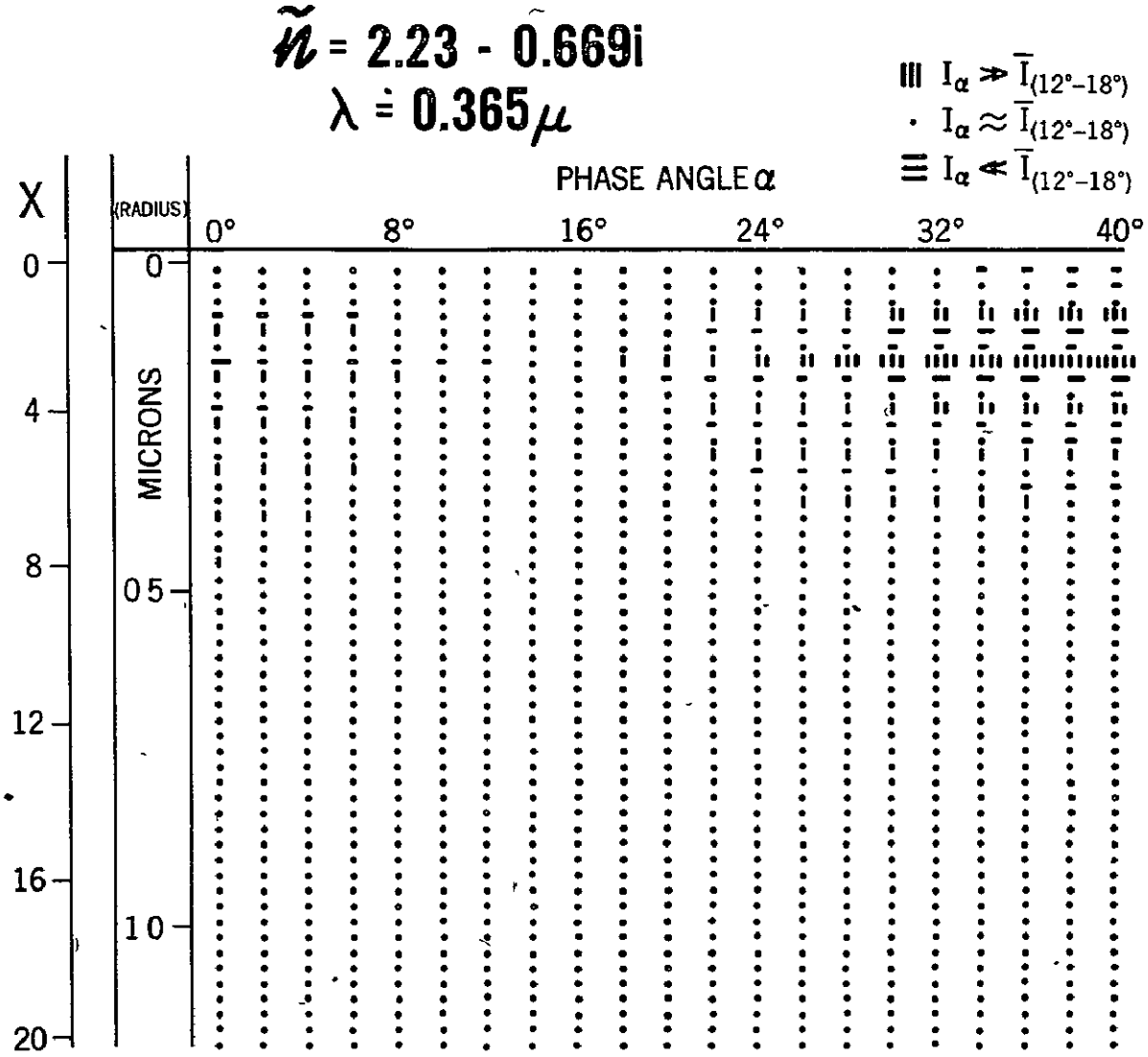

Figure 8. Same as Figure 6, except $\tilde{n} = 2.23 - 0.669i$, $\lambda = 0.365$ micron.

(I1+I2) FOR PARTICLE RADIUS VS. PHASE ANGLE
INDEX OF REFRACTION = 1.55

SIZE PARAM. X	WAVELENGTH U(.36) RADII (MICRON)	V(.55)	I(.83)	PHASE ANGLE (DEG) 0	2	4	6	8	10	12	14	16	18	20	22	24	26	28	30	32	34	36	38	40
0.4	0.023	0.035	0.053	0	0	0	0	0	0	0	0	0	0	0	0	0	0	0	0	0	0	0	0	0
0.8	0.046	0.070	0.106	0	0	0	0	0	0	0	0	0	0	0	0	0	0	0	0	0	0	0	0	0
1.2	0.069	0.105	0.159	0	0	0	0	0	0	0	0	0	0	0	0	0	0	0	0	0	0	0	0	0
1.6	0.092	0.140	0.211	0	0	0	0	0	0	0	0	0	0	0	0	0	0	0	0	0	0	0	0	0
2.0	0.115	0.175	0.264	1	1	1	1	1	1	1	1	1	1	1	1	1	1	1	1	1	1	1	1	0
2.4	0.138	0.210	0.317	1	1	1	1	1	1	1	1	1	1	1	1	1	1	1	1	1	1	1	1	1
2.8	0.160	0.245	0.370	2	2	2	1	1	1	1	1	1	1	1	1	1	1	1	1	1	1	1	1	1
3.2	0.183	0.280	0.423	6	6	6	6	6	6	6	5	5	5	5	5	4	4	4	4	4	4	4	4	4
3.6	0.206	0.315	0.476	4	4	4	4	4	3	3	3	3	3	3	3	3	3	3	3	3	4	4	5	5
4.0	0.229	0.350	0.528	16	15	15	15	14	13	12	12	11	10	9	9	8	8	8	8	8	8	8	9	9
4.4	0.252	0.385	0.581	15	15	14	14	13	12	11	11	10	9	9	9	9	10	10	11	11	12	12	12	12
4.8	0.275	0.420	0.634	30	30	29	27	24	22	19	17	15	14	13	13	14	15	16	17	18	19	19	18	18
5.2	0.298	0.455	0.687	41	40	39	36	34	30	27	24	22	20	19	19	19	19	19	19	19	18	16	14	12
5.6	0.321	0.490	0.740	66	64	60	55	48	40	34	28	25	24	25	27	31	34	37	38	38	36	32	27	21
6.0	0.344	0.525	0.793	70	69	65	59	52	45	38	33	29	27	26	26	27	27	27	25	22	18	14	10	6
6.4	0.367	0.560	0.845	163	159	146	128	107	85	67	53	46	44	47	52	57	59	58	53	45	34	23	14	7
6.8	0.390	0.595	0.898	79	77	70	61	51	41	34	30	30	32	36	39	41	41	37	32	24	17	11	7	6
7.2	0.413	0.630	0.951	300	290	252	221	173	128	90	65	53	51	55	61	63	60	51	37	23	10	3	1	5
7.6	0.435	0.665	1.004	75	72	64	54	44	37	35	39	46	55	61	64	61	53	42	30	19	12	9	9	11
8.0	0.458	0.700	1.057	368	352	309	247	179	118	73	47	39	43	51	56	54	45	31	16	6	3	6	13	21
8.4	0.481	0.735	1.110	108	104	94	81	69	63	63	68	75	80	78	70	57	40	25	14	9	8	10	12	13
8.8	0.504	0.770	1.162	370	349	294	219	141	80	43	33	42	59	71	73	64	47	29	16	10	11	15	17	16
9.2	0.527	0.805	1.215	206	198	177	150	123	104	93	89	85	78	65	48	29	15	7	5	8	11	13	11	9
9.6	0.550	0.840	1.268	396	369	297	204	119	64	49	65	95	119	123	108	79	49	26	15	13	13	11	7	3
10.0	0.573	0.875	1.321	422	398	335	254	181	132	110	105	101	89	66	39	18	7	7	12	15	14	10	8	11
10.4	0.596	0.910	1.374	465	427	331	217	131	100	120	166	202	203	168	113	62	30	20	22	25	22	14	10	14
10.8	0.619	0.945	1.427	720	657	497	310	170	115	135	184	210	188	129	63	20	9	20	32	33	23	12	9	17
11.2	0.642	0.980	1.480	217	199	158	124	124	161	214	249	242	192	120	56	21	14	24	34	35	30	24	23	24
11.6	0.665	1.015	1.532	247	225	170	111	76	76	103	133	147	134	102	64	34	17	12	13	14	15	14	13	11
12.0	0.688	1.050	1.585	154	146	130	118	124	144	166	170	150	108	62	28	14	19	31	42	45	40	29	17	8
12.4	0.710	1.085	1.638	292	270	216	159	128	131	156	178	177	147	98	50	18	6	9	19	25	24	17	9	5
12.8	0.733	1.120	1.691	141	132	111	96	100	123	150	161	147	112	71	42	34	42	55	60	53	35	16	4	3
13.2	0.756	1.155	1.744	451	415	327	234	179	174	196	209	188	133	67	19	3	16	38	52	49	32	14	7	13
13.6	0.779	1.190	1.797	196	179	143	123	141	187	229	236	201	143	88	54	45	53	62	58	38	14	1	8	29
14.0	0.802	1.225	1.849	700	622	437	252	158	169	224	249	209	123	43	10	29	71	100	95	60	22	7	20	40
14.4	0.825	1.261	1.902	101	91	82	117	207	315	376	349	251	139	66	46	56	64	53	29	12	12	26	39	40
14.8	0.848	1.296	1.955	132	118	119	201	366	517	544	422	239	116	103	153	185	157	89	30	9	17	33	38	30
15.2	0.871	1.331	2.008	144	137	138	185	282	379	405	332	198	79	29	45	78	87	63	34	24	35	46	40	20
15.6	0.894	1.366	2.061	208	175	134	191	370	565	630	512	303	148	118	164	186	136	52	4	18	60	78	59	25
16.0	0.917	1.401	2.114	163	151	145	198	308	402	396	279	129	42	55	115	148	123	68	33	30	37	30	10	1
16.4	0.940	1.436	2.166	178	142	115	231	494	734	758	545	266	111	119	178	167	84	17	27	84	110	77	25	6
16.8	0.963	1.471	2.219	143	124	114	187	335	450	427	280	132	89	144	200	179	100	33	16	29	30	16	10	22
17.2	0.985	1.506	2.272	178	131	101	266	592	823	744	428	148	83	168	219	160	69	44	79	96	59	12	6	37
17.6	1.008	1.541	2.325	1	9	121	414	725	786	565	310	232	279	278	177	67	22	23	26	23	25	29	26	16
18.0	1.031	1.576	2.378	203	146	112	298	632	797	615	270	90	171	313	310	177	67	55	71	47	10	17	57	72
18.4	1.054	1.611	2.431	186	170	215	437	732	841	654	343	156	143	168	123	45	15	37	58	52	39	36	28	12
18.8	1.077	1.646	2.483	204	136	108	351	725	836	565	237	197	381	468	323	117	34	54	58	28	28	61	66	31
19.2	1.100	1.681	2.536	595	493	404	616	973	1030	663	228	75	156	208	135	51	39	56	51	42	46	41	20	12
19.6	1.123	1.716	2.589	111	68	131	506	938	973	605	297	336	494	436	193	35	51	101	84	51	51	47	20	15
20.0	1.146	1.751	2.642	1309	958	500	733	1337	1361	684	130	198	472	427	161	25	50	58	27	39	66	43	20	54
20.4	1.169	1.786	2.695	21	33	231	719	1127	1031	584	305	350	412	274	90	58	127	147	97	45	20	10	20	40
20.8	1.192	1.821	2.748	669	425	154	425	902	887	447	236	434	577	386	109	15	42	43	22	24	29	28	42	57

Figure 9. Same as Figure 4, except n = 1.55

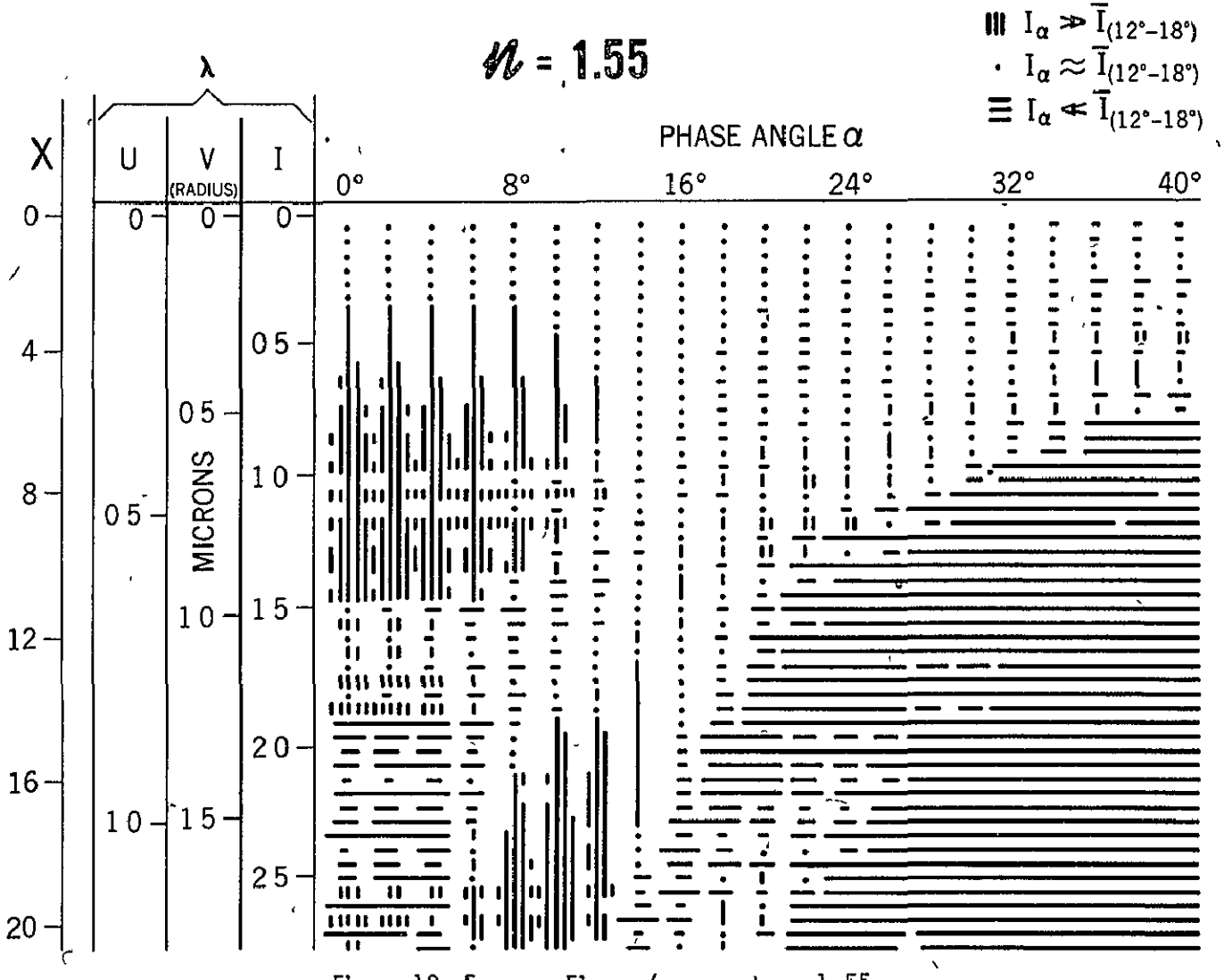

Figure 10. Same as Figure 6, except n = 1.55

(I1+I2) FOR PARTICLE RADIUS VS. PHASE ANGLE
INDEX OF REFRACTION = 1.65

SIZE PARAM X	WAVELENGTH U(.36)	V(.55)	I(.83)	PHASE ANGLE (DEG) 0	2	4	6	8	10	12	14	16	18	20	22	24	26	28	30	32	34	36	38	40
	RADII (MICRON)																							
0.4	0.023	0.035	0.053	0	0	0	0	0	0	0	0	0	0	0	0	0	0	0	0	0	0	0	0	0
0.8	0.046	0.070	0.106	0	0	0	0	0	0	0	0	0	0	0	0	0	0	0	0	0	0	0	0	0
1.2	0.069	0.105	0.159	0	0	0	0	0	0	0	0	0	0	0	0	0	0	0	0	0	0	0	0	0
1.6	0.092	0.140	0.211	0	0	0	0	0	0	0	0	0	0	0	0	0	0	0	0	0	0	0	0	0
2.0	0.115	0.175	0.264	1	1	1	1	1	1	1	1	1	1	1	1	1	1	1	1	1	1	1	1	1
2.4	0.138	0.210	0.317	1	1	1	1	1	1	1	1	1	1	1	1	1	1	1	1	1	1	1	1	1
2.8	0.160	0.245	0.370	4	4	4	4	4	4	3	3	3	3	3	3	3	3	3	3	3	3	3	3	3
3.2	0.183	0.280	0.423	10	10	10	10	9	9	9	8	8	8	7	7	7	6	6	6	6	6	6	6	7
3.6	0.206	0.315	0.476	9	9	9	9	9	8	8	7	7	6	6	5	5	5	5	5	5	6	6	6	7
4.0	0.229	0.350	0.528	42	42	41	39	37	35	32	29	26	23	21	19	17	15	14	14	13	13	12	12	12
4.4	0.252	0.385	0.581	22	22	21	20	19	17	15	14	12	11	11	10	10	11	12	13	14	14	15	15	14
4.8	0.275	0.420	0.634	97	96	92	86	79	70	60	51	42	34	28	22	19	16	15	14	14	14	14	13	12
5.2	0.298	0.455	0.687	62	61	58	54	49	43	37	33	29	26	25	24	25	25	26	26	25	23	20	17	13
5.6	0.321	0.490	0.740	148	145	137	124	107	89	71	54	40	29	22	18	17	17	18	20	20	19	18	15	12
6.0	0.344	0.525	0.793	204	199	187	167	144	119	95	75	60	50	44	41	39	38	34	30	23	16	9	4	1
6.4	0.367	0.560	0.845	172	168	154	133	109	84	61	44	32	26	25	27	30	33	34	32	28	22	16	12	9
6.8	0.390	0.595	0.898	463	449	408	348	277	205	139	87	51	31	23	23	25	27	25	20	12	6	1	0	3
7.2	0.413	0.630	0.951	143	138	125	106	85	65	49	39	35	35	37	39	39	36	31	25	19	14	12	12	12
7.6	0.435	0.665	1.004	404	390	350	291	222	153	94	49	21	7	4	6	9	11	11	9	7	5	5	5	7
8.0	0.458	0.700	1.057	149	145	133	116	96	78	62	51	43	37	32	28	24	20	17	15	15	14	13	12	9
8.4	0.481	0.735	1.110	426	407	355	280	197	120	60	21	3	1	0	14	20	22	21	18	15	13	10	7	4
8.8	0.504	0.770	1.162	415	397	348	282	213	156	115	90	74	60	45	31	19	15	17	24	30	30	24	14	6
9.2	0.527	0.805	1.215	706	664	551	397	242	118	44	17	22	39	53	57	53	46	42	39	35	28	17	6	1
9.6	0.550	0.840	1.268	499	476	414	326	235	156	100	68	54	49	46	39	29	18	10	4	3	4	7	10	12
10.0	0.573	0.875	1.321	207	197	169	133	99	77	68	70	76	81	79	70	56	40	25	14	7	6	7	10	13
10.4	0.596	0.910	1.374	518	492	421	329	233	153	101	76	70	70	67	57	40	22	9	3	6	14	23	28	28
10.8	0.619	0.945	1.427	221	214	194	168	141	120	107	101	99	95	87	72	53	34	18	10	9	14	18	20	17
11.2	0.642	0.980	1.480	576	542	461	331	217	135	97	93	106	115	109	86	55	28	15	16	28	40	43	36	21
11.6	0.665	1.015	1.532	481	456	390	308	237	193	174	166	153	126	86	46	17	4	7	16	24	25	21	14	10
12.0	0.688	1.050	1.585	604	555	431	292	196	169	196	233	241	207	145	83	44	32	37	43	39	26	11	3	6
12.4	0.710	1.085	1.638	631	597	503	401	307	248	216	194	162	114	61	20	3	10	29	43	43	33	20	13	15
12.8	0.733	1.120	1.691	472	437	351	258	204	203	238	269	265	217	144	79	41	31	35	34	23	9	3	11	26
13.2	0.756	1.155	1.744	986	916	738	530	367	282	254	235	190	120	53	18	22	46	61	54	32	15	16	29	40
13.6	0.779	1.190	1.797	649	597	473	352	294	307	344	346	286	184	88	33	23	33	37	27	14	12	23	35	36
14.0	0.802	1.225	1.849	1801	1620	1182	726	451	392	435	434	333	184	74	43	63	76	55	21	7	25	54	65	49
14.4	0.825	1.261	1.902	805	746	606	467	390	374	366	314	214	105	34	18	33	46	42	31	26	30	31	22	8
14.8	0.848	1.296	1.955	1822	1607	1094	577	300	296	410	459	369	205	74	27	34	40	25	11	18	42	54	42	19
15.2	0.871	1.331	2.008	1021	942	751	548	410	341	291	218	126	52	22	29	44	49	44	39	36	27	13	4	9
15.6	0.894	1.366	2.061	2042	1779	1166	587	323	367	497	506	361	171	49	14	20	26	28	36	45	39	23	16	30
16.0	0.917	1.401	2.114	1243	1129	855	571	385	296	243	180	113	67	48	42	41	46	56	57	41	19	10	21	34
16.4	0.940	1.436	2.166	2299	1980	1267	659	459	563	653	542	301	106	36	41	53	57	65	66	44	17	22	62	92
16.8	0.963	1.471	2.219	3477	2962	1825	881	563	644	657	435	168	54	70	82	55	54	96	118	78	24	21	54	62
17.2	0.985	1.506	2.272	1451	1277	912	651	619	675	613	397	163	44	42	78	91	80	58	35	20	26	44	50	35
17.6	1.008	1.541	2.325	2210	1884	1168	584	423	537	598	457	221	66	38	65	70	45	21	17	27	37	36	25	18
18.0	1.031	1.576	2.378	1254	1129	857	633	544	513	421	252	96	35	64	113	120	82	37	19	25	31	22	12	19
18.4	1.054	1.611	2.431	2731	2321	1430	726	555	703	750	532	224	53	56	105	92	32	1	30	74	79	47	26	38
18.8	1.077	1.646	2.483	1125	1013	764	552	461	433	369	245	128	91	126	162	139	73	26	26	42	37	22	27	41
19.2	1.100	1.681	2.536	4187	3456	1910	766	557	818	861	531	150	13	95	183	140	33	9	92	151	103	34	53	111
19.6	1.123	1.716	2.589	2052	1693	1019	692	795	864	614	260	106	146	184	131	59	30	33	29	16	13	29	43	33
20.0	1.146	1.751	2.642	2014	1695	1154	1027	1279	1315	863	299	72	159	243	179	79	55	73	61	29	28	54	59	52
20.4	1.169	1.786	2.695	1775	1505	1005	789	904	959	714	362	185	181	165	75	11	29	65	56	35	40	48	27	6
20.8	1.192	1.821	2.748	1637	1407	1024	947	1107	1050	630	211	128	262	304	186	73	51	50	24	22	58	74	42	16

Figure 11. Same as Figure 4, except $n = 1.65$

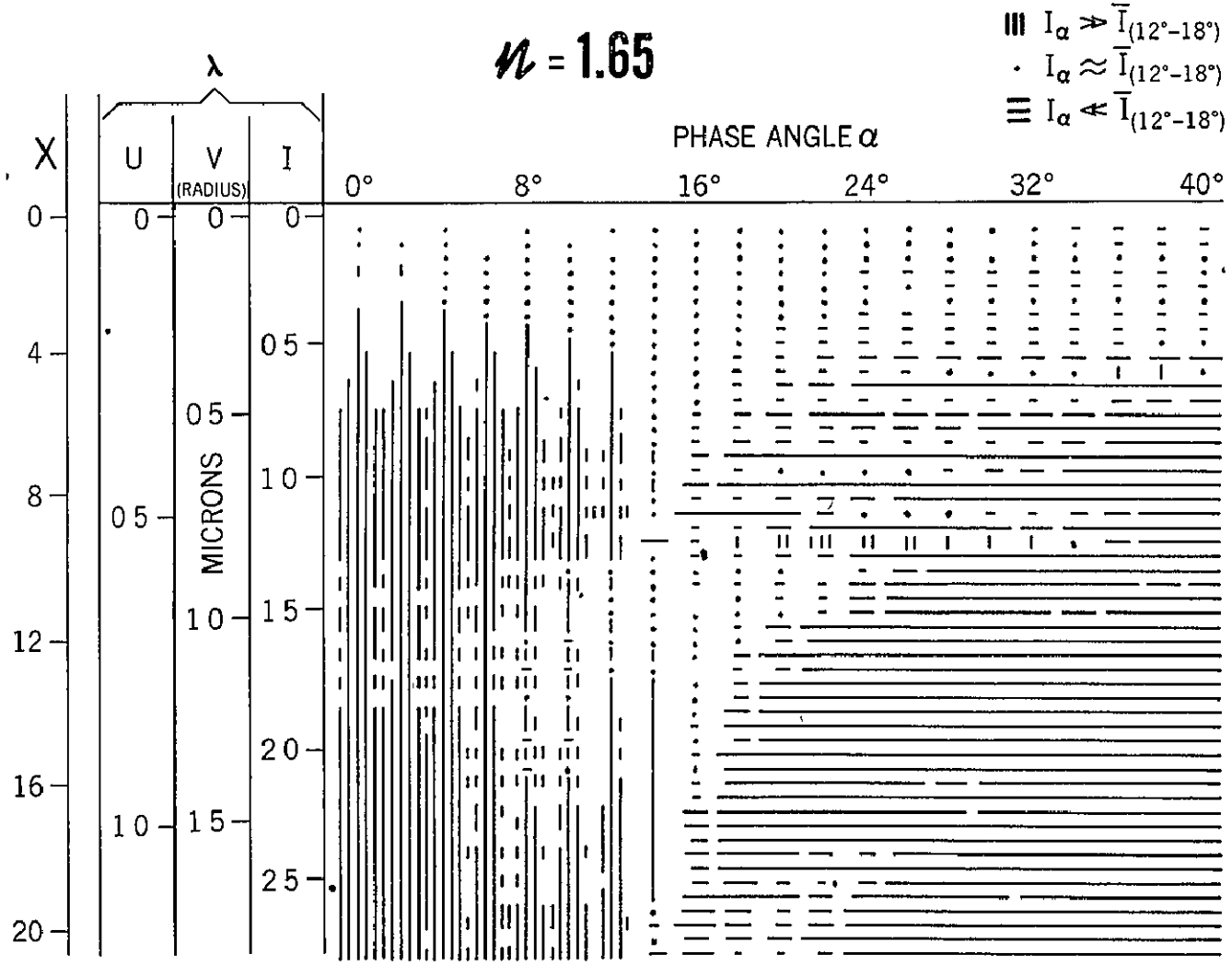

Figure 12. Same as Figure 6, except n = 1.65

(I1+I2) FOR PARTICLE RADIUS VS. PHASE ANGLE
INDEX OF REFRACTION = 1.75

SIZE PARAM. X	WAVELENGTH V(.36) RADII (MICRON)	V(55)	I(83)	PHASE ANGLE (DEG) 0	2	4	6	8	10	12	14	16	18	20	22	24	26	28	30	32	34	36	38	40
0.4	0.021	0.035	0.053	0	0	0	0	0	0	0	0	0	0	0	0	0	0	0	0	0	0	0	0	0
0.8	0.040	0.070	0.106	0	0	0	0	0	0	0	0	0	0	0	0	0	0	0	0	0	0	0	0	0
1.2	0.060	0.105	0.159	0	0	0	0	0	0	0	0	0	0	0	0	0	0	0	0	0	0	0	0	0
1.6	0.092	0.140	0.211	0	0	0	0	0	0	0	0	0	0	0	0	0	0	0	0	0	0	0	0	0
2.0	0.115	0.175	0.264	1	1	1	1	1	1	1	1	1	1	1	1	1	1	1	1	1	1	1	1	1
2.4	0.138	0.210	0.317	2	2	2	2	2	2	2	2	2	1	1	1	1	1	1	1	1	1	2	2	2
2.8	0.160	0.245	0.370	7	7	7	7	7	7	7	6	6	6	6	6	5	5	5	5	5	5	5	5	5
3.2	0.183	0.280	0.423	12	12	12	12	11	11	10	9	9	8	7	7	6	6	6	5	5	5	5	6	6
3.6	0.206	0.315	0.476	29	29	28	27	26	24	23	21	19	18	16	15	14	13	12	12	12	12	12	12	12
4.0	0.229	0.350	0.528	41	40	39	37	35	32	29	26	23	20	17	15	13	12	11	11	11	11	11	11	11
4.4	0.252	0.385	0.581	112	111	106	99	90	79	68	57	46	37	29	24	20	19	18	19	20	22	23	23	23
4.8	0.275	0.420	0.634	85	84	81	76	69	62	54	46	39	33	28	24	21	19	18	17	16	15	14	12	10
5.2	0.298	0.455	0.687	172	168	158	143	123	101	78	56	38	23	12	6	4	4	7	11	14	16	18	17	16
5.6	0.321	0.490	0.740	112	110	105	98	88	78	67	56	47	40	33	28	24	20	16	13	9	6	3	1	0
6.0	0.344	0.525	0.793	206	201	185	161	132	101	71	46	26	13	6	5	7	10	14	16	16	15	13	10	8
6.4	0.367	0.560	0.845	415	395	279	241	196	152	113	85	66	57	53	52	50	44	36	26	16	9	5	6	10
6.8	0.390	0.595	0.898	320	310	280	236	185	134	89	55	33	23	20	22	24	24	23	19	15	13	14	17	21
7.2	0.413	0.630	0.951	259	251	230	198	160	120	84	55	33	20	13	10	10	11	12	11	10	8	7	5	4
7.6	0.435	0.665	1.004	146	143	133	117	98	79	60	44	31	22	16	13	12	13	14	16	17	16	14	11	8
8.0	0.458	0.700	1.057	190	184	168	144	116	89	65	46	33	26	21	19	18	17	16	16	14	13	11	9	7
8.4	0.481	0.735	1.110	471	451	398	322	241	168	114	80	63	56	52	46	37	26	17	12	9	10	11	11	10
8.8	0.504	0.770	1.162	609	577	490	370	244	136	62	23	11	15	23	30	34	35	35	33	27	18	9	2	2
9.2	0.527	0.805	1.215	460	444	402	341	272	207	154	116	93	80	70	61	49	34	19	8	2	3	9	18	26
9.6	0.550	0.840	1.268	201	195	177	151	123	95	74	60	52	51	51	50	46	39	30	23	18	17	18	19	18
10.0	0.573	0.875	1.321	578	558	502	420	330	245	176	127	96	78	65	51	35	19	7	2	7	18	30	39	40
10.4	0.596	0.910	1.374	411	393	343	276	209	155	121	105	97	91	79	62	44	31	24	25	28	30	27	19	11
10.8	0.619	0.945	1.427	943	801	688	533	375	244	155	106	82	68	52	33	16	7	10	21	33	38	35	24	13
11.2	0.642	0.980	1.480	1018	960	807	606	414	273	193	160	146	128	97	62	38	32	42	56	61	52	33	16	10
11.6	0.665	1.015	1.532	912	860	721	537	360	223	140	99	78	60	41	25	18	22	31	37	33	22	10	6	11
12.0	0.688	1.050	1.585	2316	2132	1651	1057	543	225	105	106	133	131	96	54	30	29	38	44	39	29	19	14	12
12.4	0.710	1.085	1.638	871	818	676	493	319	190	113	77	62	53	47	44	43	40	32	19	8	5	12	24	31
12.8	0.733	1.120	1.691	3037	2749	2025	1188	536	183	67	55	58	53	47	49	52	50	43	33	23	22	31	41	39
13.2	0.756	1.155	1.744	1017	945	760	533	333	198	124	88	72	71	82	95	96	75	43	19	17	31	41	35	16
13.6	0.779	1.190	1.797	2323	2123	1632	1032	529	226	103	74	68	56	48	51	57	53	40	31	37	50	54	39	17
14.0	0.802	1.225	1.849	2223	2012	1478	858	384	158	131	178	195	156	93	46	31	33	36	31	23	14	7	5	9
14.4	0.825	1.261	1.902	1548	1438	1152	794	473	252	137	91	73	58	39	21	13	18	31	42	42	30	16	10	17
14.8	0.848	1.296	1.955	1923	1747	1302	782	376	171	132	165	187	166	118	71	44	38	41	37	23	7	4	20	43
15.2	0.871	1.331	2.008	1125	1068	914	703	485	302	179	119	102	96	77	49	35	44	61	61	39	17	18	39	55
15.6	0.894	1.366	2.061	3543	3130	2127	1053	329	49	48	131	191	203	164	92	37	40	80	90	47	4	24	92	127
16.0	0.917	1.401	2.114	2518	2270	1666	1013	565	372	316	262	168	80	46	59	76	64	34	15	24	45	54	43	26
16.4	0.940	1.436	2.166	2082	1903	1458	958	587	396	314	248	158	70	25	27	45	49	36	25	29	36	30	15	8
16.8	0.963	1.471	2.219	3091	2754	1943	1100	575	415	424	389	262	128	71	78	79	44	7	16	62	94	79	40	22
17.2	0.985	1.506	2.272	1059	1076	1109	1085	916	614	329	200	195	174	96	52	99	160	143	77	44	51	47	26	33
17.6	1.008	1.541	2.325	4632	3957	2407	947	186	73	243	392	382	223	57	29	105	124	51	28	126	207	150	47	52
18.0	1.031	1.576	2.378	3726	3344	2427	1464	802	459	276	146	73	67	83	74	53	57	83	86	51	18	23	49	50
18.4	1.054	1.611	2.431	3262	2837	1868	974	543	486	488	377	211	100	56	33	21	37	67	70	41	24	40	61	51
18.8	1.077	1.646	2.483	7650	6550	4060	1801	719	530	484	269	74	64	127	113	61	74	127	124	60	22	34	38	11
19.2	1.100	1.681	2.536	3558	3119	2114	1164	643	477	406	297	175	87	40	26	40	58	50	26	24	47	59	42	25
19.6	1.123	1.716	2.589	8113	6772	3802	1258	239	290	444	313	100	18	45	87	111	111	87	63	60	55	27	7	34
20.0	1.146	1.751	2.642	4197	3710	2563	1403	674	385	310	258	170	80	42	66	95	78	37	31	56	57	28	21	50
20.4	1.169	1.786	2.695	7320	6023	3224	981	239	390	508	344	132	32	37	103	158	135	72	66	99	78	21	34	98
20.8	1.192	1.821	2.748	9986	8291	4731	1985	962	706	408	195	236	269	156	92	149	157	74	41	70	54	21	65	128

Figure 13. Same as Figure 4, except $n = 1.75$

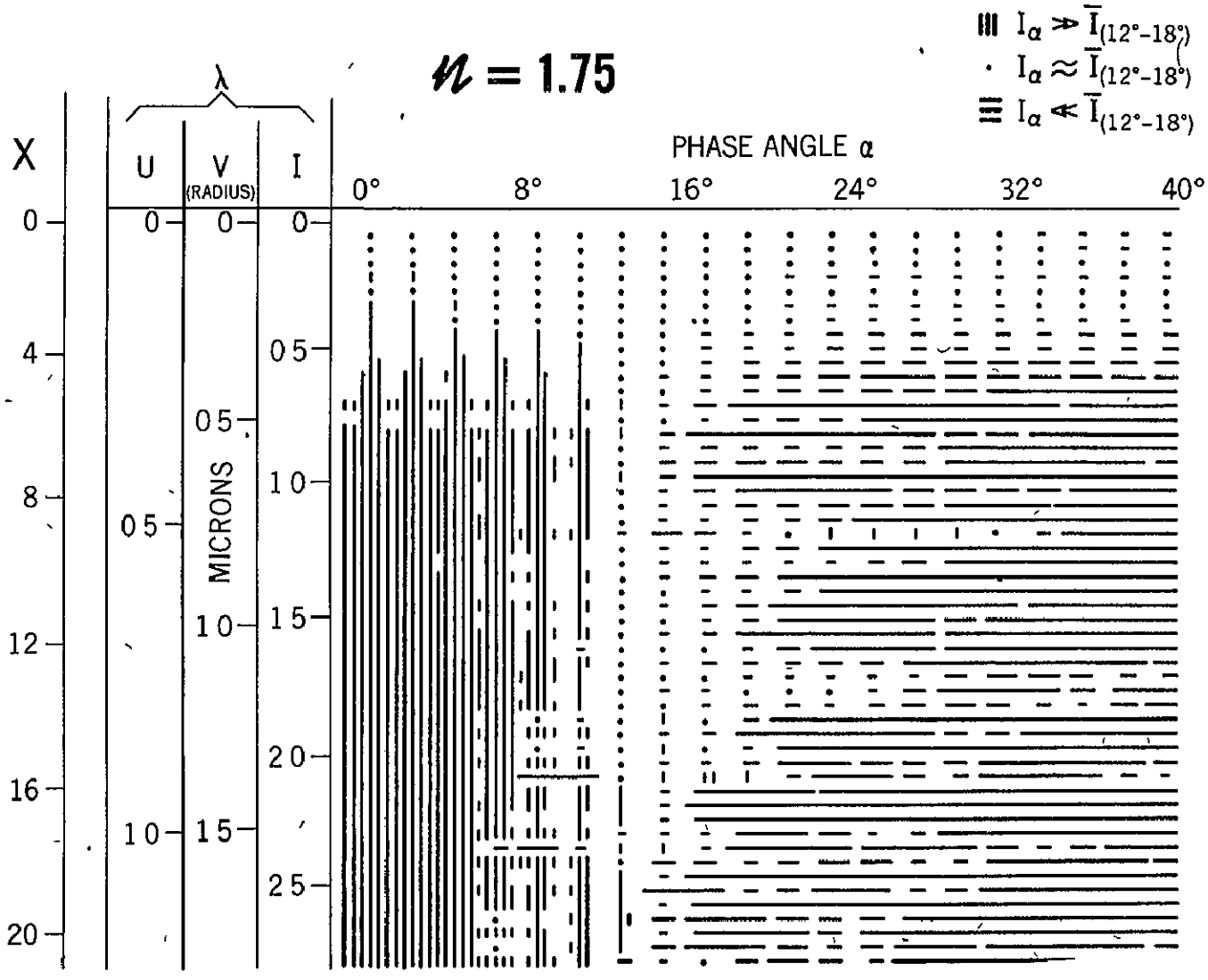

Figure 14. Same as Figure 6, except n = 1 75

submicron particles at each of the three wavelengths shown, we see that the opposition effect is most pronounced in the U, less significant in the V, and much reduced in the I for spheres of refractive index 1.65--- which is just what the photometric observations of Mars show (see Figure 3).

The opposition effect for $\underline{n} = 1.75$ is even more pronounced than for $\underline{n} = 1.65$. A comparison of Figures 11 and 13 shows that the intensities at small phase angles for $\underline{n} = 1.75$ are much greater than those computed for $\underline{n} = 1.65$. At the same time, the intensities at larger phase angles are about the same for both. Therefore, it is not surprising that the schematic diagram for $\underline{n} = 1.75$ (Figure 14) has almost continuous vertical lines between 6° and 0° phase angle, indicating an opposition effect of $1^{m}.25$ or greater (see Table 2).

The displays for $\underline{n} = 1.65$ and 1.75 are typical for real indices of refraction from 1.60 to 2.00. From $\underline{n} = 2.00$ to 2.40, the effect gradually decreases.

CHAPTER V

INTEGRATED INTENSITIES FOR PARTICLE-SIZE DISTRIBUTIONS

Having investigated the light scattering behavior of single spherical particles of various sizes and refractive indices, our next step was to compute the intensity of the light scattered by groups of such particles. To do this we used several particle-size distributions based on the general function given by Deirmendjian (1964) as typical of terrestrial clouds and hazes:

$$N(a) = q\, a^{\delta} e^{-b a^{\gamma}} \tag{14}$$

where $N(a)\,da$ is the number density of aerosol particles with radii between a and $a+da$; q, δ, b, and γ are positive constants.

Two forms of Equation (14) are obtained. When $\delta \neq 0$, the constant b was chosen so as to make $N(a)$ a maximum at particle radius a_0. The normalized form of Equation (14) is then

$$N(a) = C \cdot \left(\frac{a}{a_0}\right)^{\delta} \cdot e^{-\frac{\delta}{\gamma}\left(\frac{a}{a_0}\right)^{\gamma}} \tag{15}$$

with the normalizing factor

$$C = \frac{D}{\Gamma\left(\frac{\delta+1}{\gamma}\right)} \cdot \frac{\gamma}{a_0} \cdot \left(\frac{\delta}{\gamma}\right)^{\frac{\delta+1}{\gamma}} \tag{16}$$

δ and γ are parameters determining the width of the distribution function, and $\Gamma(x)$ is the gamma function. The normalization was chosen so that

$$\int_0^\infty N(a)\,da = D \tag{17}$$

where D is the total aerosol number density.

When $\delta = 0$, Equation (14) is a negative exponential:

$$N(a) = \frac{D\gamma e^{-\left(\frac{a}{a_0}\right)^\gamma}}{a_0 \Gamma\left(\frac{1}{\gamma}\right)} \tag{18}$$

where a_0 and γ determine the width of the distribution function.

Figure 15 shows five particle size distributions $N(a)$, which are typical of those used in the Mie calculations to obtain integrated scattering intensities. Although calculations were made for distributions over particle radii ranging up to 4μ, for this study we have considered only submicron particles. The two types of normalized distributions which have been used are illustrated in Figure 15: negative exponentials and skewed gaussian-type distributions. Table 3 gives the values of the parameters used to produce these distributions. Distribution E1 emphasizes very small particles by including primarily radii less than 0.4μ. E2 is much broader, thus including larger particles. The three skewed gaussian-type distributions shown in Figure 15 peak at 0.2, 0.4 and 0.6μ.

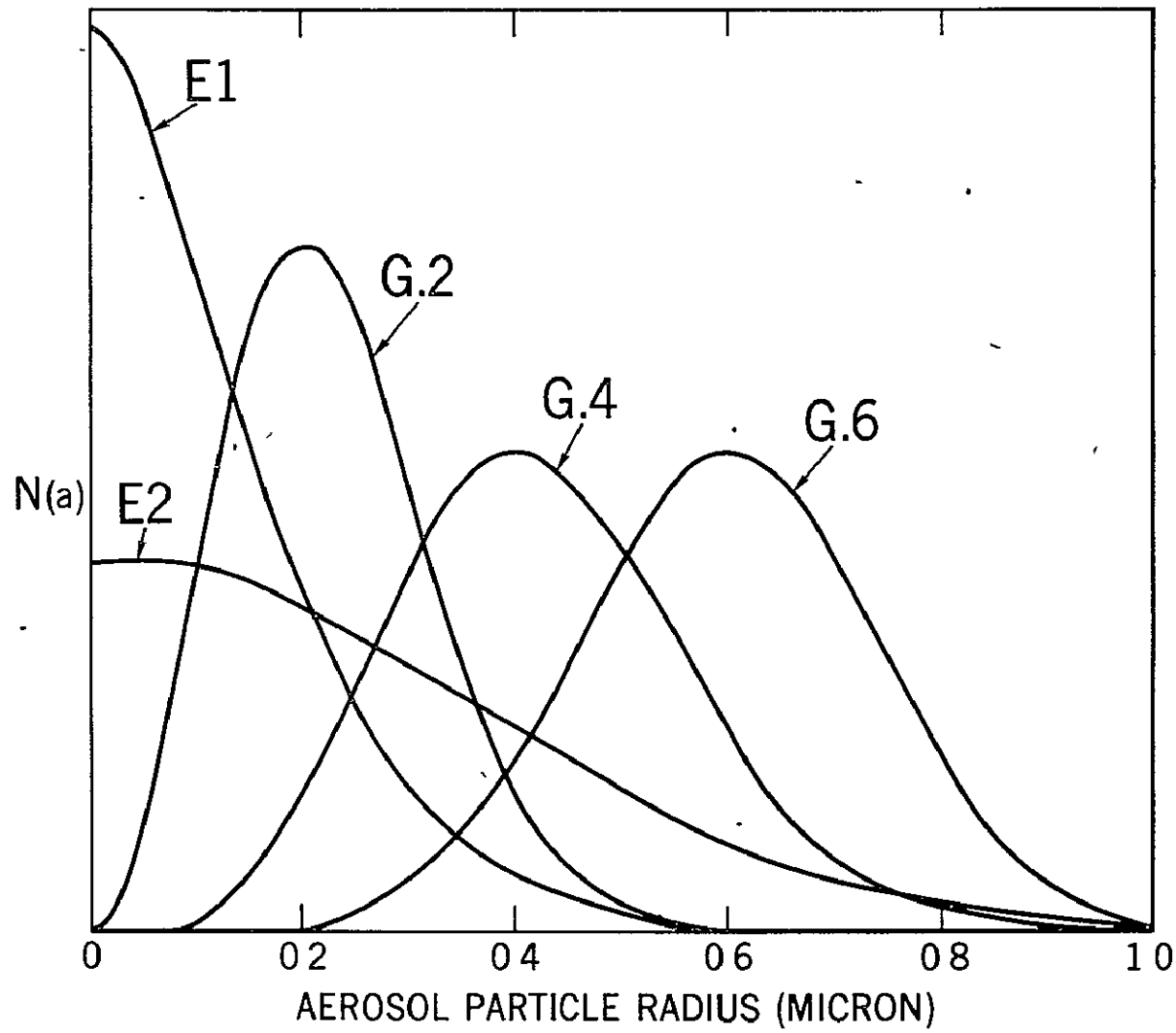

Figure 15. Typical particle size distributions used in calculations of integrated scattering intensities.

TABLE 3

PARAMETERS USED IN PARTICLE-SIZE DISTRIBUTIONS

Distribution	δ	γ	a_0
E1	0	1.5	0.2μ
E2	0	2.0	0.5
G.2	2	2.0	0.2
G.4	4	2.0	0.4
G.6	6	3.0	0.6

Equation (3) gives the intensity I of the light scattered by a single particle of radius a. For a particle-size distribution $N(a)$, the integrated intensity I' is

$$I' = \frac{I_0 \lambda^2}{8\pi^2 r^2} \int_{a=0}^{a_{max}} \left[i_1(x, \tilde{n}, \theta) + i_2(x, \tilde{n}, \theta) \right] N(a)\, da \qquad (19)$$

This expression has been evaluated for various indices of refraction and various submicron particle-size distributions, with particle radius increments of 0.01μ. These integrated intensities were plotted in terms of magnitudes and are shown in Figures 16 - 19. The λ^2 factor of Equation (19) has been included in the calculations, since each curve

is for a specific wavelength. The normalization which was made for the single particle schematic displays in Figures 6, 8, 10, 12, and 14 has not been used in these calculations of integrated intensities, however.

Figure 16 shows the integrated intensities for $n = 1.35$. Calculations are displayed for five wavelengths and two particle-size distributions as a function of phase angle. From Figure 6, the single-particle display for $n = 1.35$, we recall that only a few very small particles showed a slight opposition enhancement, whereas particles of a little larger size showed an enhancement at larger phase angles. This behavior is reflected in the results obtained with Distribution E1 of Figure 15. When larger particles are weighted more heavily, as with Distribution G.6, the brightness curves peak at phase angles greater than 10°, as could be expected from examining the contributions from single particles.

Thus it appears that aerosols of refractive index 1.35 cannot produce the required opposition effect. Other distributions of larger-size particles were also incapable of simulating the observations. The same was generally true for all real refractive indices from 1.20 to 1.50.

Figure 17 shows the integrated intensities for $n = 1.55$. The same negative exponential and skewed gaussian-type distributions have been used here as in Figure 16. As suggested by the single-particle display for $n = 1.55$ (Figure 8), there is a definite increase in the integrated intensity for both distributions from around 10° phase angle.

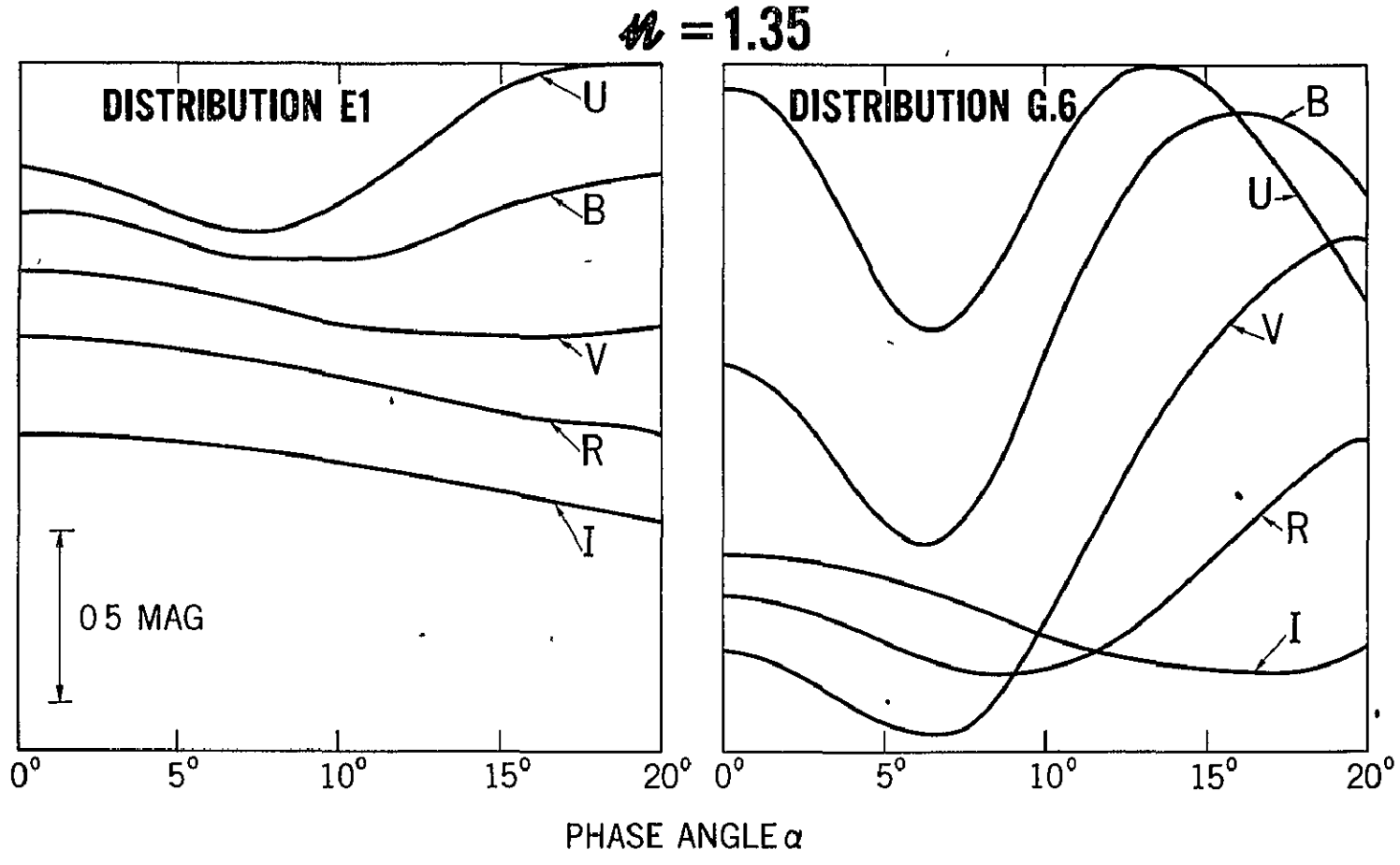

Figure 16. Integrated scattering intensities for aerosols of refractive index 1.35, as obtained with two particle size distributions Intensity in magnitudes is plotted versus phase angle for the five wavelengths. 0.36 (U), 0.43 (B), 0 55 (V), 0 67 (R), and 0 83 (I) micron.

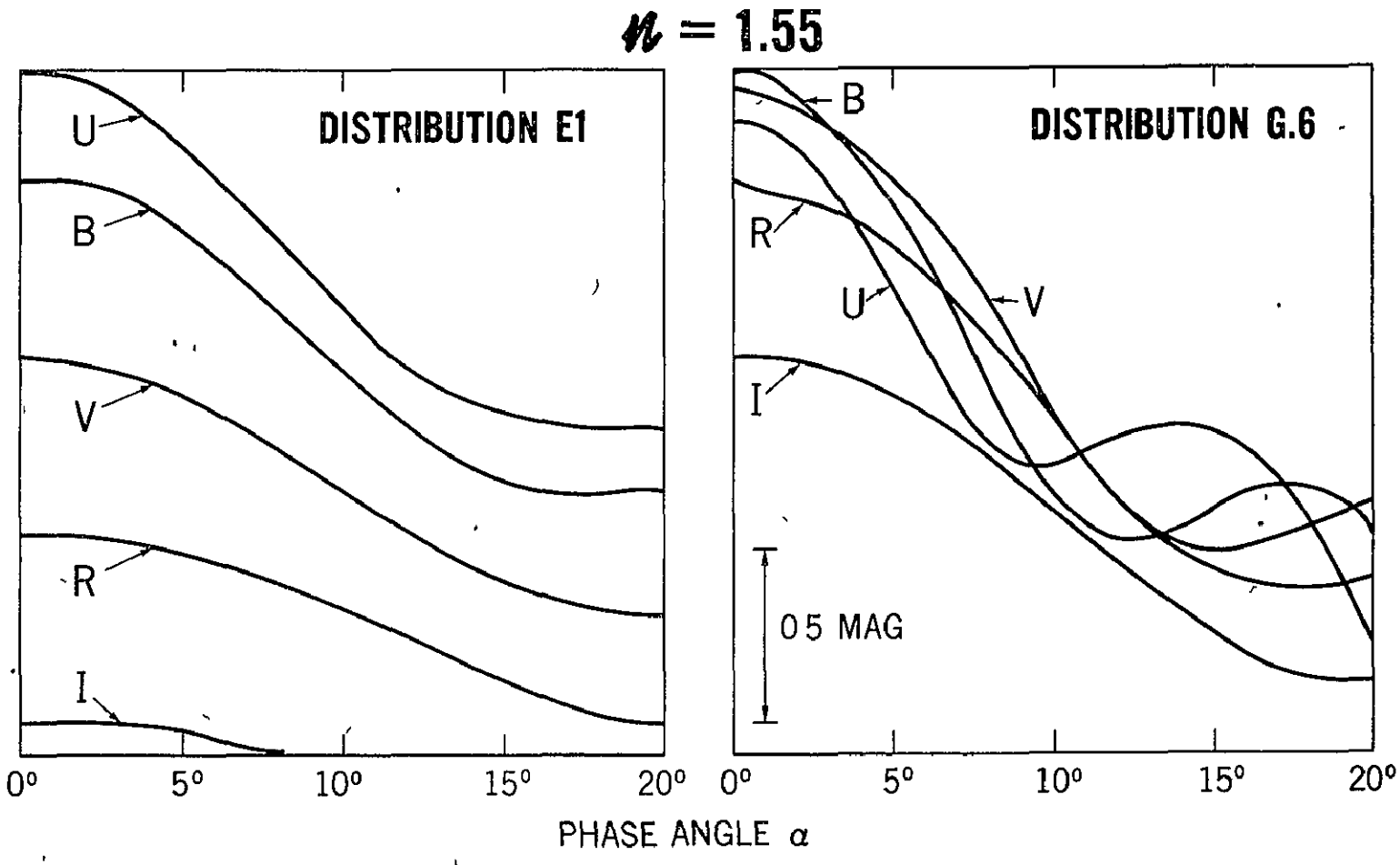

Figure 17. Same as Figure 16, except $n = 1.55$

Even more impressive examples of an opposition effect are seen in Figures 18 - 19, where $\underline{n} = 1.65$ and 1.75, respectively. The increase in intensity from 15° to 0° in the ultraviolet for Distribution G.4 is approximately $2^{m}.0$, or about a factor of 6, for both of these refractive indices.

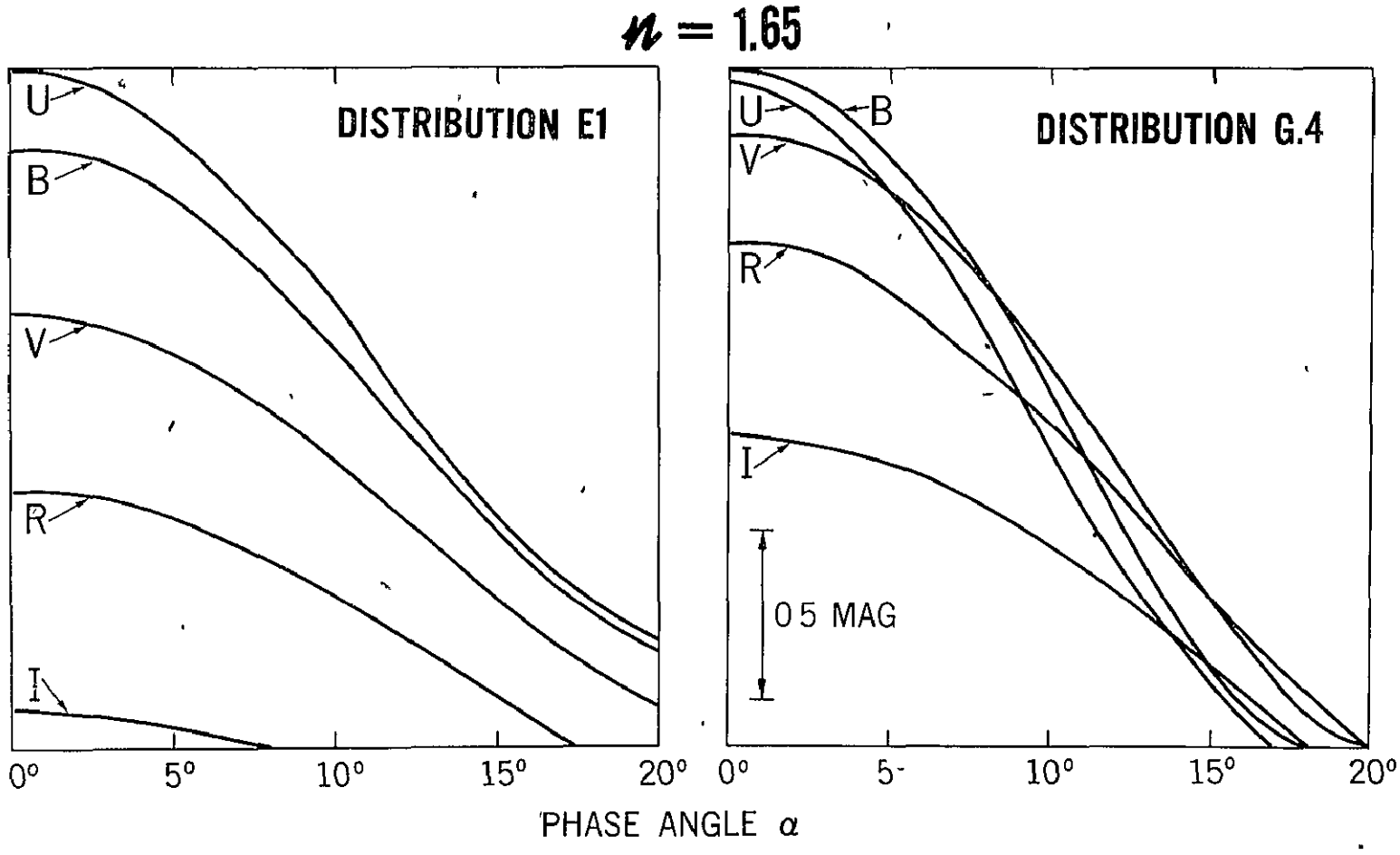

Figure 18. Same as Figure 16, except n = 1.65

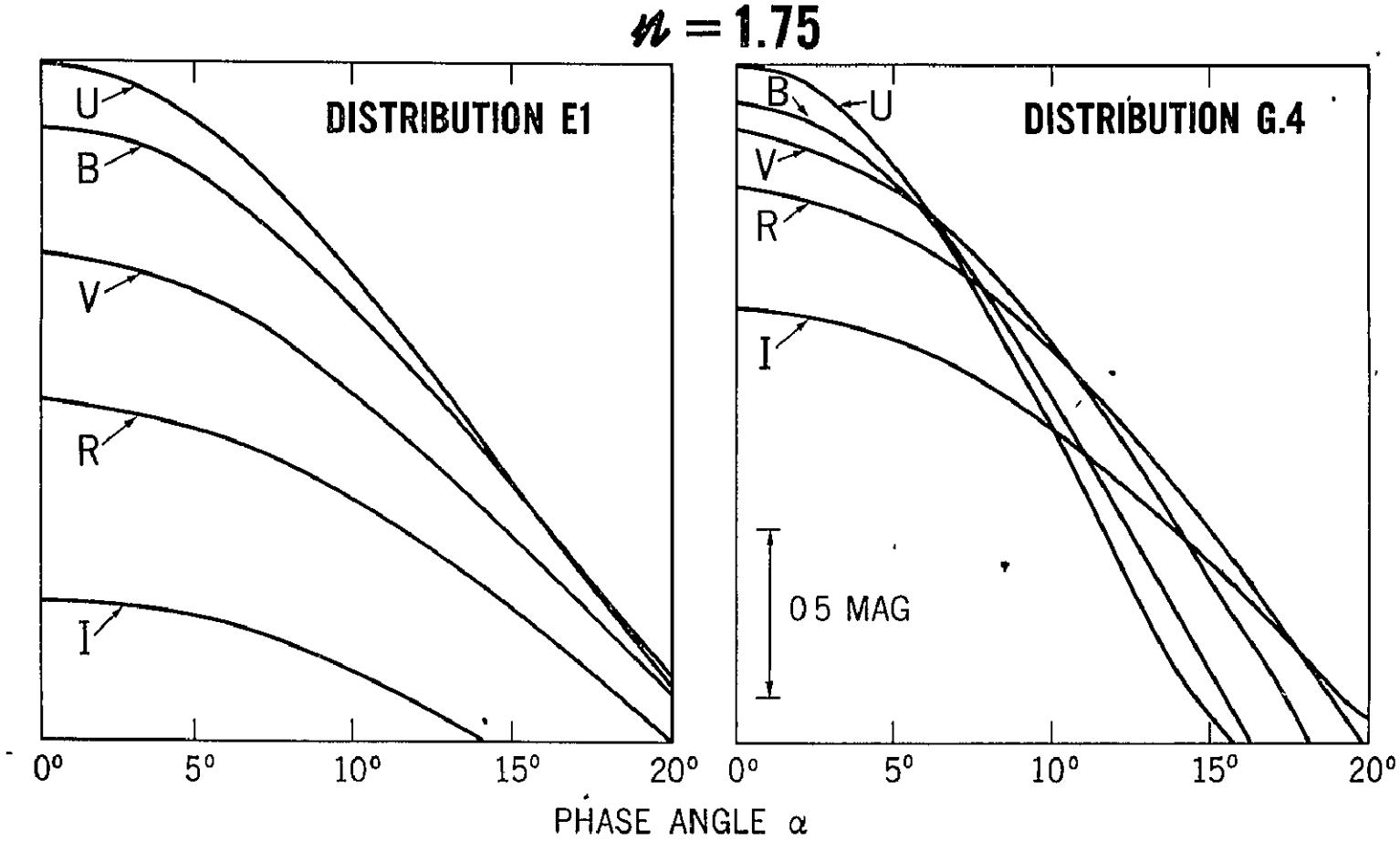

Figure 19. Same as Figure 16, except n = 1.75

CHAPTER VI

MODELS OF SURFACE PLUS AEROSOLS AND COMPARISON WITH OBSERVATIONS

Having found that refractive indices of 1.55 or greater could produce a significant enhancement in intensity at small phase angles, we next generated a model consisting of a surface brightness function plus a brightness contribution by atmospheric aerosols. At longer wavelengths, where the Martian albedo is higher and where surface markings are more clearly visible, it is reasonable to assume that the observed brightness comes almost entirely from the surface and that the brightness contribution by aerosols is negligible. As suggested by de Vaucouleurs (1968), we took the lunar photometric function developed by Hapke (1963) and modified it to fit the observed Martian brightness-phase curve at these longer wavelengths.

The scattering law as given by Hapke (1963) for the integrated brightness $I(\alpha)$ of the whole Moon as a function of phase angle α is as follows:

$$I(\alpha) = I(0) \cdot \left[1 - \sin\frac{\alpha}{2} \tan\frac{\alpha}{2} \ln\left(\cot\frac{\alpha}{4}\right)\right] \frac{\sin\alpha + (\pi-\alpha)\cos\alpha}{\pi} \cdot B(\alpha, g), \qquad (20)$$

where $B(\alpha, g)$ is the retrodirective function which expresses the opposition effect:

$$B(\alpha, g) = 1 - \frac{\tan\alpha}{4g}\left(1 - e^{-g/\tan\alpha}\right)\left(3 - e^{-g/\tan\alpha}\right) \cdot \qquad (21)$$

The parameter q determines the sharpness of the opposition effect. In Hapke's theory, q is closely related to the degree of compaction of the surface.

Equation (20) was modified to fit the observed Martian phase curves at longer wavelengths by replacing $B(\alpha, g)$ by its cube root and setting the compaction parameter $q = 0.2$. We then assumed that the phase curve for the surface would have the same shape (when plotted on a magnitude scale) in all colors; that is, the surface phase curves would be wavelength-independent; only the albedo would change, in accordance with the wavelength-dependence of the Martian albedo observations. This meant that in the model, the surface brightness would increase by 30% from 16° to 0° phase angle at all wavelengths.

Any attempt to separate the brightness contributions of the atmosphere and the surface of Mars based on our present knowledge must necessarily involve certain assumptions. In this connection, it is useful to see what conclusions can be drawn from laboratory measurements of the angular scattering of various materials. O'Leary and Rea (1968) have measured the phase functions of several sample substances of interest in connection with the Martian surface: fine limonite, fine and coarse goethite, fine and coarse hematite, fine and coarse siderite, and four synthetic mixtures containing varying amounts of magnetite, goethite, silica, hematite and hornblende. The fine particle radii of the samples were less than 19 μ, the coarse goethite

particle radii ranged from 125 to 250 μ, and the coarse siderite and hematite radii were between 250 and 500 μ. The measurements were made at wavelengths of 0.43, 0.56, and 0.68 μ.

We replotted the O'Leary-Rea data on semi-logarithmic paper and compared the three phase curves for each sample at phase angles of 15° and less in order to determine the relative wavelength-dependence of these substances. The percentage increase in reflectivity from phase angles of 15° to 1° is greater at the shorter wavelength for eight of the eleven samples; however, the coarse hematite and the coarse goethite exhibit a greater increase in reflectivity at the longer wavelength than at the shorter one. (The coarse siderite shows the greatest percentage increase in reflectivity for the wavelength of 0.56 μ.)

This suggests that although many substances may exhibit a greater reflectivity at shorter wavelengths than at longer ones, this is not always the case; in particular, the phenomenon may be a function of particle size. Because of the uncertainties in the composition and mineralogy of the Martian surface, the dominant particle size and texture of the material, and, therefore, the photometric properties of the surface, we have assumed for this model that the surface phase curves are wavelength-independent. Should this not be the case, some of the conclusions of this paper could be altered significantly.

Having modified Equation (20) so that it would give the same shape

(on a magnitude scale) as the observational phase curves for Mars at longer wavelengths, we used this same phase curve to represent the surface at all other wavelengths by incorporating an overall surface albedo constant appropriate to each wavelength. The initial choice of these albedo surface constants was based on our knowledge of the wavelength variation of the albedo of Mars (see Table 1).

In addition to the five free parameters for the surface albedo at the five wavelengths under consideration, there is one other free parameter in the model: the aerosol number density. It is obvious that this parameter must be the same for all wavelengths; however, the brightness, or albedo, of the aerosols, which depends directly on the aerosol number density, will vary with wavelength, due to the wavelength-dependence of the scattering intensities for a given index of refraction. We have already seen this from the light scattering calculations for single particles (Chapter IV) and for particle-size distributions (Chapter V).

We next made a number of test calculations in an effort to find the combination of these six parameters---the surface albedo constants for the five wavelengths and the aerosol number density---which would best fit the observed data for Mars. The results are shown in Figure 20 for aerosols of refractive index 1.65. The thin lower curves are the final assumed surface functions for I, V, B and U (R has been omitted for simplicity). Note that they all have the same shape on a

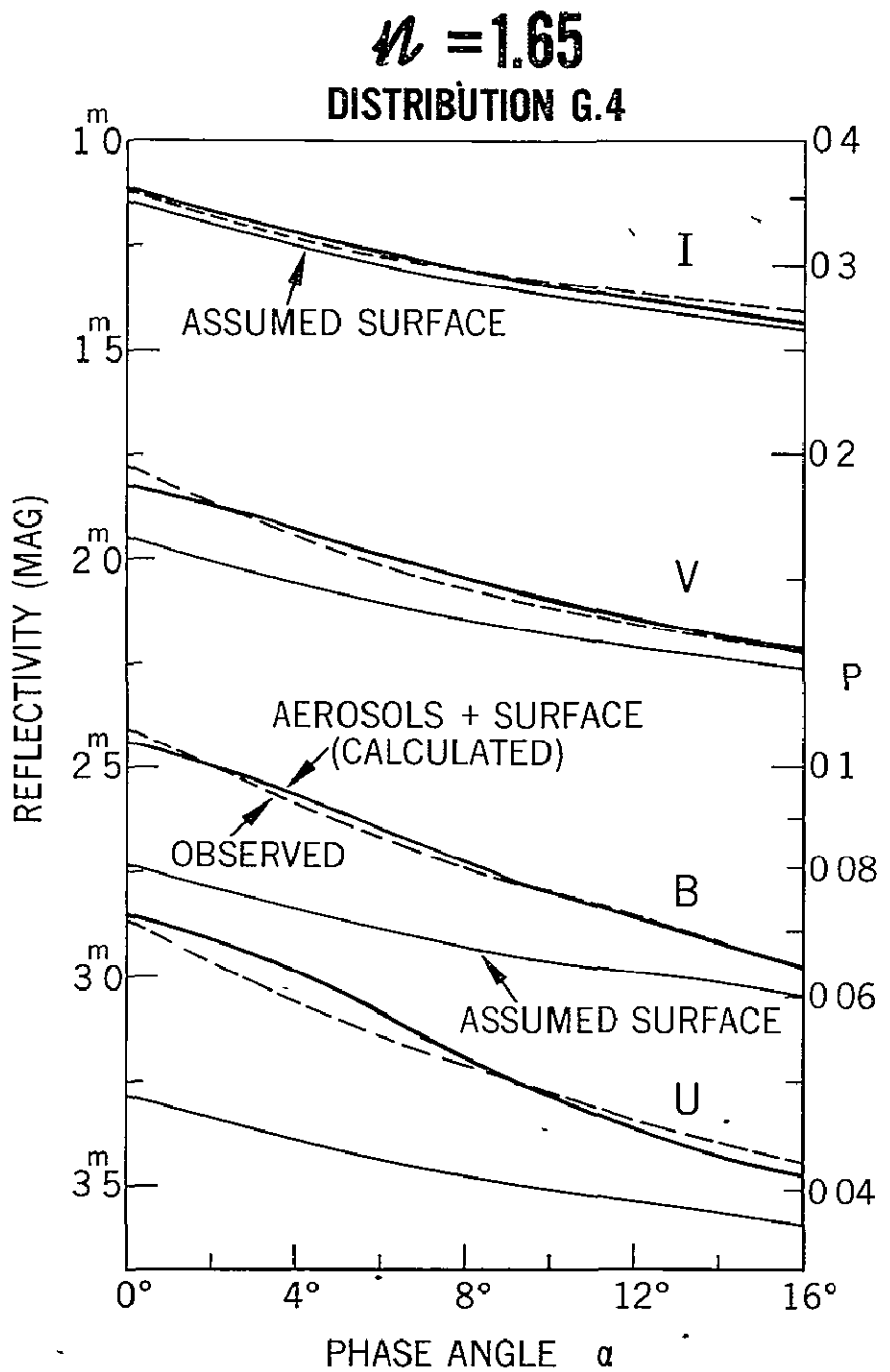

Figure 20. Comparison of model with Mars observations. For each wavelength, the thin lower curve is the assumed surface reflectivity, the heavy upper curve is the calculated brightness from the surface plus aerosols of refractive index 1.65, and the broken curve is the Martian observational data.

magnitude scale and differ only in albedo. The upper heavy solid curves in Figure 20 represent the sum of the reflectivities of the surface plus aerosols for refractive index 1.65, using a skewed gaussian-type particle distribution peaked at 0.4μ (Distribution G.4; see Figures 15 and 18). At shorter wavelengths, where the albedo and surface contrast are greatly reduced, the atmospheric aerosols are seen to play a significant role. The calculated phase curves are in reasonable agreement with the observations, which are shown as dashed lines.

In Chapter V we showed that spherical particles with various indices of refraction greater than 1.50 could produce an opposition effect. To further illustrate this, additional models were developed for aerosols of refractive index 1.55 and 1.75. Figure 21 shows the results which were obtained for $\underline{n}$ = 1.75 and Distribution G.4. The fit to the observational data does not appear to be quite as close as for $\underline{n}$ = 1.65; however, it might be possible to get a better fit with additional variations of the free parameters. No fit could be found, however, for aerosols having refractive index 1.50 or less.

Although the calculated phase curves of surface plus atmospheric aerosols shown in Figures 20 and 21 are in reasonable agreement with the observations, one should bear in mind that there was a good deal of arbitrariness in obtaining this fit. It is by no means a unique solution to the problem. It does show, nonetheless, that the presence of a small amount of atmospheric aerosols, with the proper index of

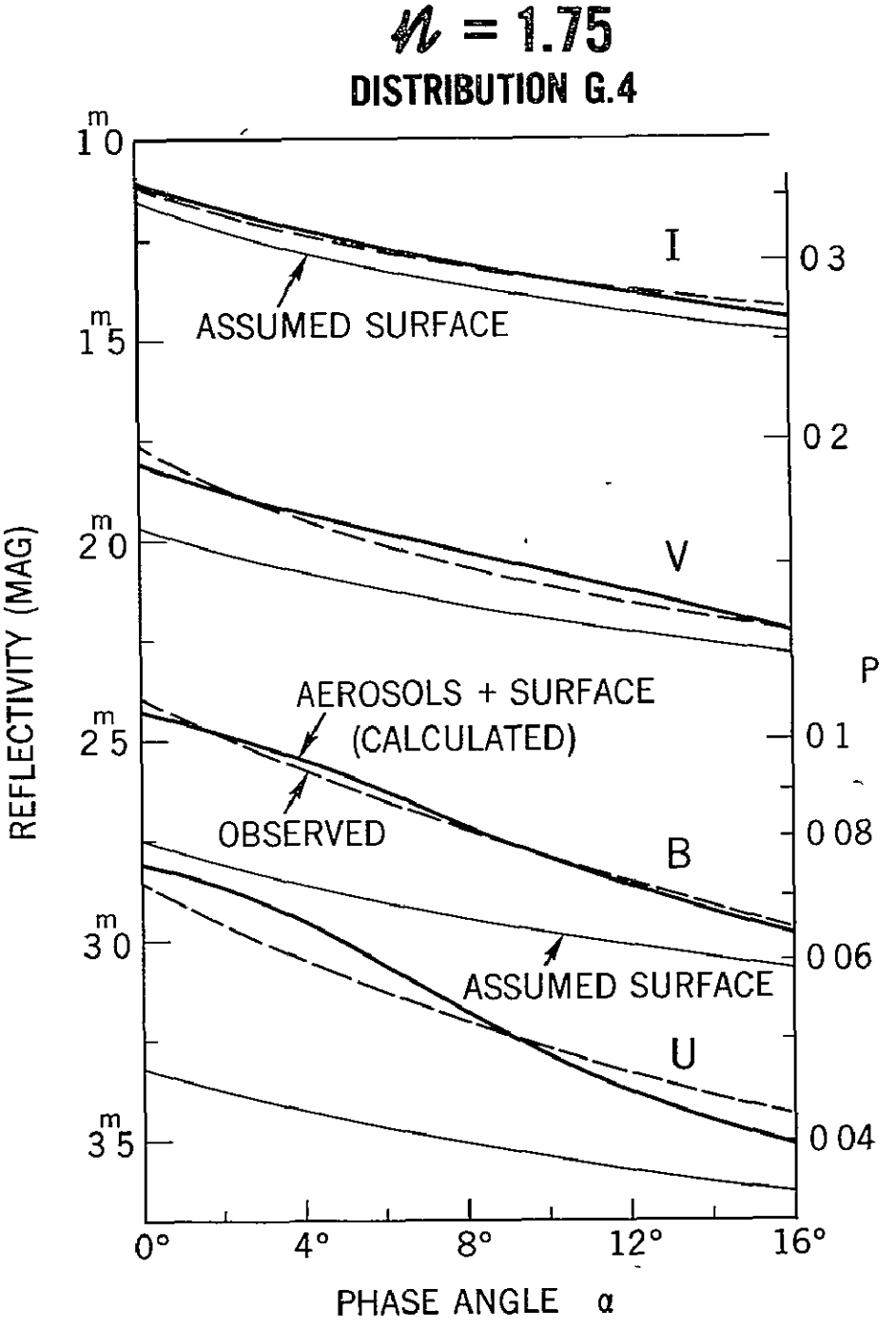

Figure 21. Same as Figure 20, except refractive index of aerosols is 1.75

refraction, could provide the observed increased opposition effect for Mars in the ultraviolet, where the albedo is very low, but at the same time make a negligible contribution in the infrared, where the surface albedo is high.

Tables 4 and 5 show the reflectivities of the surface ($\underline{P}_s$) and the aerosols ($\underline{P}_{ar}$) for U, V and I at phase angles 0° and 16°, and the ratio of the aerosol brightness to the surface brightness, as obtained from the models for $\underline{n}$ = 1.65 and 1.75, respectively. Note that $\underline{P}_{ar}/\underline{P}_s$ reaches a maximum of 0.49 in the ultraviolet at opposition for aerosols of $\underline{n}$ = 1.65, but falls off rapidly both with increasing wavelength and increasing phase angle. For refractive index 1.75, the maximum brightness ratio is 0.69. Since $\underline{P}_{ar}$ rarely exceeds 3% in either case, the atmosphere is optically thin at all wavelengths, and the assumption of single scattering is justified.

The reflectivities in Figures 2, 3, 20, and 21 and in Tables 4 and 5 are normalized so as to be equal at 0° phase angle to the geometric albedo, i.e., the ratio of the average intensity of the planet at full phase to the intensity (I_L) of a perfectly diffusing circular disk (Lambert surface) at the same distance from the Sun and normal to the incident radiation. Thus

$$P(\alpha) = \frac{I(\alpha)}{I_L(0°)} \qquad (22)$$

TABLE 4

REFLECTIVITY OF SURFACE AND AEROSOLS, AS OBTAINED WITH MODEL FOR $\underline{N}$ = 1.65 AND DISTRIBUTION G.4

α	λ	$\underline{P}_s$	$\underline{P}_{ar}$	$(\underline{P}_s + \underline{P}_{ar})$	$\underline{P}_{ar}/\underline{P}_s$
0°	U	0.048	0.024	0.072	0.49
	V	0.166	0.021	0.187	0.13
	I	0.350	0.009	0.359	0.03
16°	U	0.036	0.004	0.040	0.12
	V	0.124	0.005	0.129	0.04
	I	0.261	0.004	0.265	0.02

TABLE 5

SAME AS TABLE 4, EXCEPT $\underline{N}$ = 1.75

α	λ	$\underline{P}_s$	$\underline{P}_{ar}$	$(\underline{P}_s + \underline{P}_{ar})$	$\underline{P}_{ar}/\underline{P}_s$
0°	U	0.045	0.031	0.076	0.69
	V	0.162	0.026	0.188	0.16
	I	0.344	0.015	0.359	0.04
16°	U	0.035	0.005	0.040	0.14
	V	0.123	0.008	0.131	0.06
	I	0.260	0.008	0.268	0.03

Since we have assumed an optically thin atmosphere with no multiple scattering or atmospheric absorption of reflected light from the surface, Equation (22) holds for the partial reflectivity of the aerosol layer as well as the total reflectivity. One can thereby determine the absolute aerosol number densities in the Martian atmosphere needed to give the model aerosol reflectivities in Tables 4 and 5.

Let D be the columnar density of aerosols (particles/cm^2) in the Martian atmosphere, with a particle-size distribution such that $D \cdot n(a)\,da$ represents the columnar density of particles with radii between a and $a + da$ ($\int n(a)\,da = 1$). If the radius of Mars is b, there are a total of $4\pi b^2 D$ aerosol particles over the entire surface, and exactly half of these are illuminated and visible at opposition. Thus, from Equation (19), the total intensity of the light reflected from the aerosol layer is given by

$$I = 2\pi b^2 D \cdot \frac{I_o \lambda^2}{8\pi^2 r^2} \cdot \int (i_1 + i_2)\, n(a)\, da \qquad (23)$$

where r is the distance to the planet. The intensity of a Lambert disk of radius b (area $A = \pi b^2$) at 0° phase angle is

$$I_L(0^\circ) = \frac{I_o A}{\pi r^2} = \frac{I_o b^2}{r^2} \qquad (24)$$

Thus

$$P_{ar} = \frac{I}{I_L(0^\circ)} = \frac{\lambda^2 D}{4\pi} \int (i_1 + i_2)\, n(a)\, da \qquad (25)$$

and

$$D = \frac{4\pi P_{ar}}{\lambda^2 \int (\iota_1 + \iota_2)\, n(a)\, da} \qquad (26)$$

with dimensions of (cm^{-2}), since $\underline{P}$, $(\iota_1 + \iota_2)$ and $n(a)da$ are dimensionless.

This equation was used, together with the computer printouts of the integrated intensities corresponding to Figure 18, to compute that a columnar particle density of 0.8×10^6 spherical aerosol particles/cm^2 ($\underline{n} = 1.65$, Distribution G.4) was required to give the reflectivities of the aerosol layer shown in Table 4. For aerosols of refractive index 1.75, the columnar particle density required to give the reflectivities in Table 5 is 0.9×10^6 aerosol particles/cm^2. Assuming an average particle radius $a = 0.4\mu$ (see Distribution G.4, Figure 15) with a density of 2.5 gm/cm^3, a value typical of semitransparent minerals (see next chapter), we find that the density of aerosols required in the above model for aerosols having refractive indices of 1.65 or 1.75 corresponds to a columnar mass of about 6×10^{-7} gm/cm^2.

This number can be compared with the columnar mass of the gaseous atmosphere on Mars, which is 19 gm/cm^2 for a surface pressure of 7 mb. The mass ratio of aerosols to gaseous atmosphere for our model is therefore 3×10^{-8}, thus demonstrating that only a very small amount of aerosols is needed to produce the observed opposition effect.

CHAPTER VII

SOURCES OF MARTIAN ATMOSPHERIC AEROSOLS

Several sources can account for the presence of aerosols in a planetary atmosphere: (1) *in situ* particle formation through condensation, photochemical reactions, and coagulation of the gaseous atmospheric constituents; (2) influx of meteoric particles; and (3) upsweeping of dust from the surface of the planet.

(1) A few atmospheric aerosols which might be formed *in situ* have already been considered in the calculations for water, ice, and solid CO_2 particles; they were found to be incapable of producing the observed opposition effect. However, measurements of Mariner 6 taken at 79°N latitude at the beginning of polar night indicate that conditions in the Martian atmosphere are favorable for the condensation of CO_2 at almost all altitudes; Mariner 7 measurements taken at 58°S in daytime and 38°N at night also show that CO_2 condensation is possible at altitudes above about 25 km (Kliore *et al.*, 1969). Condensation of CO_2 is predicted for atmospheric temperatures below 150°K. The only available refractive indices for solid CO_2 at $\lambda < 0.6\mu$, as pointed out earlier, were made at $T = 195°K$ (Egan and Spagnolo, 1969). Should the refractive index be significantly higher at $T < 150°K$, the above conclusions with regard to solid CO_2 aerosols would need revision. It is highly desirable, therefore,

to have additional measurements of the refractive index of solid CO_2 at $T < 150^{\circ}K$, $\lambda < 0.6\mu$. Other gases besides CO_2 are likely to be present on Mars, since current estimates of the concentration of CO_2 range as low as 60% (Kliore et al., 1969). Therefore, the role of minor atmospheric constituents should not be ignored as possible sources of atmospheric aerosols.

(2) Since Mars is located near the asteroid belt and also since photographs of its surface by Mariners 4, 6, and 7 show what appears to be evidence of extensive meteoritic bombardment, meteoric particles may be a source of Martian atmospheric aerosols. The minerals which are present in most common meteorites have a refractive index about 1.65, a value which falls within the range of refractive indices for which the above calculations exhibit an opposition effect.

(3) Measurements of the dielectric constant of the Martian surface indicate that the abundance of limonite in the surface material is relatively low (Beck and de Wys, 1969). Comparison with terrestrial and lunar abundances indicates that the minerals to be expected in the Martian surface materials are feldspar, pyroxene, olivine, amphibole, quartz, magnetite, ilmenite, hematite, and limonite (goethite) (Beck and de Wys, 1969; P.D. Lowman, Jr., private communication). Table 6 lists typical refractive indices for these minerals (Wahlstrom, 1947). The last four are highly absorbing and could not, therefore, exhibit an opposition effect,

between wavelengths of 0.35μ and 1.0μ. Such a material would satisfy the requirements for the dust particles in the Martian atmosphere. Adams (1968) found that the reflectance spectrum of an oxidized basalt matched quite well the spectral geometric albedo curve for Mars.

Because the Martian atmospheric density is very low, one might question whether the atmosphere could support aerosols. It is interesting to note in this regard that in the Earth's stratosphere, where the density is roughly comparable to that near the surface of Mars, there exists a worldwide permanent layer of submicron aerosol particles, containing sulfur as a major constituent, with traces of iron and silicon (Junge et al., 1961). Using the average-size-distribution curve reported for these particles for altitudes above 20 km (Junge et al., 1961, Figure 23, Curve 1B, having maximum concentration for particle radii of about 0.1μ) and assuming this density distribution to be uniformly spread over an altitude range of 20 km, we compute the columnar particle density of submicron aerosols in the Earth's stratosphere to be about 10^6 particles/cm^2. This is comparable to the value calculated earlier from our models for Mars, based on the reflectivities of the aerosol layer given in Tables 4 and 5, although we assumed particle-size distributions peaked at particle radii of 0.4μ.

The third step was to generate a model consisting of a surface photometric function plus an aerosol brightness contribution. The albedo for each surface function was assigned according to the wavelength-dependence of the Martian albedo observations; however, the surface functions were chosen to have the same shape (when plotted on a magnitude scale) for all colors; that is, the surface brightness increased by 30% from 16° to 0° phase angle at all wavelengths. Should this assumption be incorrect, some of the conclusions of this study could be altered significantly.

Calculations for models having atmospheric aerosols with $\underline{n}$ = 1.55, 1.65, and 1.75 fit reasonably well with the observational data; the aerosol brightness contribution provided a significant enhancement at small phase angles in the ultraviolet, where the albedo is low, and yet at the same time made a negligible contribution in the infrared, where the surface albedo is high. A similar fit would probably be obtained with any real index between 1.55 and 1.75.

Although the fitting of the model was somewhat arbitrary and by no means a unique solution to the problem, it did show that the observed opposition effect can be produced by atmospheric aerosols with the proper index of refraction. In the model having atmospheric aerosols with $\underline{n}$ = 1.65, a columnar density of 0.8×10^6 aerosols/cm^2 with average particle radius of 0.4μ gave the required aerosol

contribution to the total reflectivity. Assuming a density of 2.5 gm/cm^3, this corresponds to a mass ratio of aerosols to gaseous atmosphere (for a Martian surface pressure of 7 mb) of 3×10^{-8}. This indicates that only a very small amount of aerosols is needed to produce the observed opposition effect.

Finally, a number of possible sources of planetary atmospheric aerosols were considered: *in situ* particle formation from gaseous atmospheric constituents; influx of meteoric particles; and upsweeping of dust from the surface of the planet. Refractive indices of representative substances in each group were discussed. The most promising candidates are semitransparent minerals, most of which have *n* between 1.55 and 1.75. This suggests that meteoric particles from outside the planet or dust from the surface of the planet may be present as atmospheric aerosols, thus producing the Martian opposition effect.

REFERENCES

Adams, J.D. (1968). Lunar and Martian surfaces: petrologic significance of absorption bands in the near-infrared. Science 159, 1453-1455.

Beck, A.J., and de Wys, E.C. (1969). Mars surface models (1968). NASA (Natl. Aeron. Space Admin.) SP-8020

Boyce, P.B. (1970). Blue haze and Mariner 6 pictures of Mars. Science 167, 907-908.

Deirmendjian, D. (1964). Scattering and polarization properties of water clouds and hazes in the visible and infrared. Appl. Optics 3, 187-196.

de Vaucouleurs, G. (1954). "Physics of the Planet Mars." Faber and Faber, London.

de Vaucouleurs, G. (1959). Multicolor photometry of Mars in 1958. Planet. Space Sci. 2, 26-32.

de Vaucouleurs, G. (1964). Geometric and photometric parameters of the terrestrial planets. Icarus 3, 187-235.

de Vaucouleurs, G. (1968). On the opposition effect of Mars. Icarus 9, 598-599.

Dollfus, A. (1961). Polarization studies of planets, in "Planets and Satellites" (Kuiper and Middlehurst, Editors), Univ. Chicago Press, Chicago, pp. 343-399.

Egan, W.G., and Becker, J.F. (1969). Determination of the complex index of refraction of rocks and minerals. Applied Optics 8, 720-721.

Egan, W.G., and Spagnolo, F.A. (1969). Complex index of refraction of bulk solid carbon dioxide. Applied Optics 8, 2359-2360.

Gehrels, T., Coffeen, T., and Owings, D. (1964). Wavelength dependence of polarization. III. The lunar surface. Astron. J. 6_ 326-852.

Glasstone, S. (1968). "The Book of Mars." NASA (Natl. Aeron. Space Admin.) SP-179.

Hapke, B.W. (1963). A theoretical photometric function for the lunar surface. J. Geophys. Res. 68, 4571-4586.

Harris, D.L. (1961). Photometry and colorimetry of planets and satellites, in "Planets and Satellites" (Kuiper and Middlehurst, Editors), Univ. Chicago Press, Chicago, pp. 272-342.

Hess, S.L. (1961). Mars as an astronautical objective. Advan. Space Sci. Technol. 3, 151-193.

Hess, S.L. (1970). Blue haze and Mariner 6 pictures of Mars. Science 167, 906-907.

Irvine, W.M., Simon, T., Menzel, D.H., Charon, G., Lecomte, G., Griboval, P., and Young, A.T. (1968a). Multicolor photoelectric photometry of the brighter planets. II. Observations from Le Houga Observatory. Astron. J. 73, 251-264.

Irvine, W.M., Simon, T., Menzel, D.H., Pikoos, C., and Young, A.T. (1968b). Multicolor photoelectric photometry of the brighter planets. III. Observations from Boyden Observatory. Astron. J. 73, 807-828.

Irvine, W.M., and Higdon, J.G. (1969). Longitudinal variations, the opposition effect and monochromatic albedos for Mars. To be published in "Proceedings of IAU Symposium 40, Planetary Atmospheres, Marfa, Texas, Oct. 26-31, 1969."

Johnson, H.L., and Gardiner, A.J. (1955). The magnitude and color of Mars during the 1954 opposition. Pub. Astron. Soc. Pacific 67, 74-77.

Junge, C.E., Chagnon, C.W., and Manson, J.E. (1961). Stratospheric aerosols. J. Meteorol. 18, 81-108

Kellogg, W.W., and Sagan, C. (1961). "The Atmospheres of Mars and Venus." Nat. Acad. Sci.-Nat. Res. Coun. Pub. 944, Wash., D.C.

Kliore, A., Fjeldbo, G., Seidel, B.L., and Rasool, S.E. (1969). Mariners 6 and 7: radio occultation measurements of the atmosphere of Mars. Science 166, 1393-1397.

Koval', I.K. (1968). Phase dependence of the brightness of Mars. Astron. Zhur. 45, 841-849; translation Soviet Astron. 12, 668-674 (1969).

Leighton, R.B., Horowitz, N.H., Murray, B.C., Sharp, R.P., Herriman, A.H., Young, A.T., Smith, B.A., Davies, M.E., Leovy, C.B. (1969). Mariner 6 and 7 television pictures: preliminary

analysis. Science 166, 49-67.

Michaux, C.M. (1967). "Handbook of the Physical Properties of the Planet Mars". NASA (Natl. Aeron. Space Admin.) SP-3030.

Mie G. (1908). Beitrage zur optik truber medien, speziell kolloidaler metallosungen. Ann. der Phys. 25, 377-445.

O'Leary, B.T. (1967a). The opposition effect of Mars. Astrophys. J. 149, L147-L149.

O'Leary, B.T. (1967b). "Mars: Visible and Near Infrared Studies and the Composition of the Surface," Ph.D. Thesis, Univ. of Calif., Berkeley.

O'Leary, B.T., and Rea, D.G. (1968). The opposition effect of Mars and its implications. Icarus 9, 405-428.

Opik, E.J. (1962). The atmospheres and surface properties of Mars and Venus, in Prog. in the Astronaut. Sci. 1, 261-342.

Opik, E.J. (1969). Mars: the changing picture. Irish Astron. J. 9, 136-148.

Slipher, E.C. (1962). "The Photographic Story of Mars" (J.S. Hall, Editor), Sky Pub. Co., Cambridge, Mass.

Tempelmeyer, K.E., and Mills, E.W., Jr. (1968). Refractive index of carbon dioxide cryodeposit. J. Appl. Phys. 39, 2968-2969.

van de Hulst, H.C. (1957). "Light Scattering by Small Particles." Wiley, New York.

Wahlstrom, E.E. (1947). "Igneous Minerals and Rocks." Wiley, New York.

Woolley, R.v.d.R. (1953). Monochromatic magnitudes of Mars in 1952. Mon. Not. Roy. Astron. Soc. 113, 521-525.

Woolley, R.v.d.R., Gottlieb, K., Heintz, W., and de Vaucouleurs, A. (1955). Monochromatic magnitudes of Mars in 1954. Mon. Not. Roy. Astron. Soc. 115, 57-59.